Handbook of Graphene

Chapter · June 2019

DOI: 10.1002/9781119468455.ch131

4 authors:

Rakesh Arul
University of Cambridge
45 PUBLICATIONS **703** CITATIONS
SEE PROFILE

Reece Oosterbeek
University of Oxford
48 PUBLICATIONS **593** CITATIONS
SEE PROFILE

Ben P P Mallett
Victoria University of Wellington
35 PUBLICATIONS **368** CITATIONS
SEE PROFILE

Cather Simpson
University of Auckland
91 PUBLICATIONS **1,699** CITATIONS
SEE PROFILE

8

Laser Direct-Writing Graphene Oxide to Graphene—Mechanisms to Applications

Rakesh Arul[1,2,3,4], Reece N. Oosterbeek[5], B.P.P. Mallett[1,2,3,4] and M. Cather Simpson[1,2,3,4]*

[1]The Photon Factory, The University of Auckland, Auckland, New Zealand
[2]The MacDiarmid Institute for Advanced Materials and Nanotechnology and The Dodd Walls Centre for Quantum and Photonic Technologies, New Zealand
[3]School of Chemical Sciences, The University of Auckland, Auckland, New Zealand
[4]Department of Physics, The University of Auckland, Auckland, New Zealand
[5]Department of Materials Science and Metallurgy, University of Cambridge, United Kingdom

Abstract

Laser reduction of graphene oxide is a simple yet highly versatile method for the rapid prototyping and fabrication of graphene-based devices. This chapter reviews the state-of-the-art in laser reduction of graphene oxide, using a variety of laser sources (pulsed and continuous wave), as well as non-laser light. A coherent picture of the mechanism underlying the complicated chemical and structural rearrangement of graphene oxide to reduced graphene oxide is summarized. The fundamental microscopic changes performed by the laser sources are correlated to the macroscopic parameters relevant for technological applications. Finally, the state-of-the-art in commercializing the laser reduced graphene oxide in the context of the broader field of graphene-based technologies is surveyed.

Keywords: Laser reduced graphene oxide, photoreduction, graphene, laser direct-writing, photochemistry, graphene technology

8.1 Introduction

Graphene has a distinguished status in condensed matter science for its many fundamentally unusual properties. In recent years, the focus of the field has broadened to investigate the myriad applications under the umbrella of "graphene-based technologies" [1]. This encompasses the use of graphene in industrial and commercial applications, where the key challenge is to reliably and reproducibly manufacture/pattern graphene. Laser reduction of graphene oxide (GO) and of other carbon-based precursors has emerged as a promising technique to marry graphene production to a science of simplicity [2].

Laser reduction holds the ability to simultaneously pattern and synthesize graphene onto a variety of surfaces, which provides it a key advantage over other techniques. In this chapter, we review the current status of this potentially quite powerful approach to achieving

**Corresponding author*: c.simpson@auckland.ac.nz

Sulaiman Wadi Harun (ed.) Handbook of Graphene: Volume 8, (237–288) © 2019 Scrivener Publishing LLC

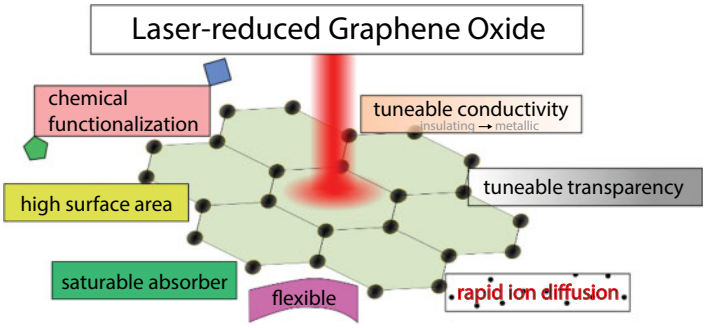

Figure 8.1 The physical and chemical properties of laser-reduced graphene oxide makes it a "materials panacea" for a variety of engineering and technology applications.

industrial-scale graphene. The chapter is broken into several sections. First, we will briefly discuss the context in which laser reduction of GO sits. We explore the features of graphene's behavior that make it exciting for novel technologies, highlight some of these technological applications, and briefly discuss methods other than photoreduction for the synthesis of graphene. The next section presents an overview of laser reduction of GO by presenting and comparing the performance of the most important experimental approaches. We follow this with a discussion of the current understanding of the mechanism of the transformation of GO to functional reduced graphene oxide (rGO) by light. We explore the main photo-physical and photo-chemical processes involved in the photoreduction of GO [3], and survey spectroscopic and computational studies in order to build a coherent picture of the timescales of various processes.

Importantly, laser reduced GO (LrGO) has a range of physical and chemical properties that make it competitive with other synthesized forms of graphene (Figure 8.1), thus enabling it to be used throughout the range of graphene-based technologies. For this reason, we critically evaluate the metrics and tools the field commonly uses to judge the quality of graphene produced by laser reduction. This "tutorial review" also correlates characterization tools to figures-of-merit for the various applications of rGO. The fundamental microscopic mechanisms of the reduction process will be correlated to the macroscopic experimental parameters that can be tuned. This section follows structure–property–processing–performance approach familiar to most materials scientists.

Finally, we discuss the state-of-the-art in the field of commercialization of LrGO technologies from 2010 to present. We evaluate examples of laser rGO technologies, and how they have progressed along the route to commercialization, leaving the confines of the research lab.

8.2 The Context—Graphene

8.2.1 Advantageous Properties of Graphene

Here we briefly describe important properties of graphene that make it such a desirable material for applications in electronics and photonics (Figure 8.2). The discovery and synthesis of graphene was awarded a Nobel Prize in 2010, and since the initial papers in the early 2000s [1], an explosion of exotic graphene behaviors has been discovered [2, 3].

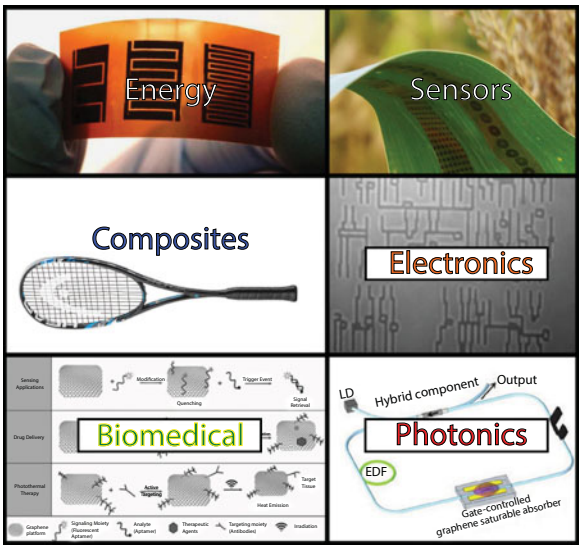

Figure 8.2 Graphene-based technologies are being developed for hundreds of applications. Here we focus on a few areas which utilize rGO's unique set of properties; *Energy*: A flexible supercapacitor. Copyright 2013 Springer Nature, reproduced from [13] with permission. *Sensors*: Photo courtesy of Liang Dong. *Composites*: A Head™ tennis racquet made from a graphene composite. *Electronics*: Reproduced from [42] under creative commons licence. *Biomedical*: Copyright 2013 John Wiley and Sons and reproduced from [43] with permission. *Photonics*: Reproduced from [44] under creative commons licence.

8.2.1.1 Electronic Properties

A single sheet of pure graphene has the best room temperature electron mobility of any material known today, up to ~10^5 cm^2 V^{-1} s^{-1} [2, 4–6]. Graphene's band structure, first calculated by Wallace in 1947 [7], shows it is a zero-band-gap semi-conductor, with electron–hole symmetry at the corners of its Brillouin zone (the *K* and *K'* points) [8, 9]. As an ambipolar semi-conductor, graphene can be readily electron- or hole-doped up to a carrier concentration of ~10^{13} cm^{-2} by chemical methods or electrical gating [2]. Typical values of the sheet conductance are ~5×10^3 S/cm for a gate voltage ~100 V [1].

Isolated sheets of pure graphene are rare occurrences, but even in the more common imperfect situations—involving rough substrates, defects, and surface adsorbates—graphene retains a remarkably high mobility and good electrical conductivity [9–12]. GO on the other hand is an electrical insulator, with in-plane conductivity values of ~1×10^{-3} S/m [13, 14]. Oxygen can form sp^3 bonds with carbon [15], localizing those electrons on the bond and opening a band gap at the chemical potential.

8.2.1.2 Optical and Photonic Properties

Graphene is an attractive material for optical and photonic applications [16]. Pristine graphene, despite being atomically thin, possesses a relatively high optical absorption of ~2.3% in the visible wavelength region. The optical absorption can be changed by altering the number of stacked layers.

Under high intensity irradiation graphene is a saturable absorber [17]. Indeed graphene has the highest known saturable absorption [18]. Saturable absorption is the decrease of light absorption in a material as the intensity of light increases [19], and is incredibly useful in passive mode locking and the generation of picosecond and sub-picosecond laser pulses [20, 21]. Graphene displays several other nonlinear optical properties, including efficient second harmonic generation [22, 23], fluorescence up-conversion [24], and a giant nonlinear Kerr index that is eight to nine orders of magnitude higher than typical dielectrics [25, 26]. This unusually high Kerr index is shared by analogous GO and laser rGO materials [27]. The linear refractive index is also tunable across a huge range from ~0.01 to ~0.35 in femtosecond laser treated GO [28].

The emission of light by graphene can be engineered through several methods, including size/shape manipulation, defect manipulation, and chemical doping of the hexagonal lattice [16, 29]. Defect states related to oxygen bonds to carbon (e.g. in GO), and localized sp^2 clusters can also introduce a bandgap [30] and create electroluminescent and photoluminescent properties in the NIR to UV region [31–33]. A counter-intuitive phenomenon that has been observed is the fluorescence quenching properties of graphene-based materials, due to its often heterogeneous nature [34, 35]. The graphitic regions of GO and rGO have been shown to quench the fluorescence of dyes [36], and have been used to suppress the fluorescence that plagues resonance Raman spectroscopy of organic molecules [37].

8.2.1.3 Electrochemical Properties

Graphene's high surface area (~2600 $m^2\ g^{-1}$ [38]) and electrical conductivity make it very well suited as an electrode for electrochemical sensing and other applications. Graphene electrodes can be made of highly oriented pyrolytic graphite/glassy carbon modified by graphene [38, 39], or directly using laser modified graphene. There are two distinct classes of structural features on graphene: the edge plane and the basal plane, which can display different electrochemical reaction kinetics/rates [38, 40, 41]. The electrochemical properties of graphene can be modified by the attachment of probes like enzymes, complexation agents, or redox active ligands (like ferrocene) [41], which allows for targeted sensing of specific analytes in solution.

8.2.2 Graphene-Based Technologies

8.2.2.1 Composites and Coatings

Graphene-containing composite materials, in which graphene is used as a dispersed reinforcing component, show exceptional promise for a variety of applications. Polymer–graphene composites have been the most heavily investigated thus far [45], showing improved mechanical strength, electrical conductivity, and thermal stability [46]. Obtaining a suitable dispersion of graphene is critical, and a number of methods have emerged to address this challenge. These include *in situ* polymerisation [47], solution intercalation [46], and melt blending [48]. Composites of semiconductors with graphene are also extremely promising as photocatalysts, with applications in the photodegradation of organic pollutants, water splitting, and CO_2 reduction [49]. Recently, graphene coatings have also garnered attention as corrosion-inhibiting coatings, due to

their excellent barrier properties and chemical stability [50, 51]. It should be noted however, that graphene is cathodic to most metals, meaning that any slight scratch or pinhole defect could dangerously accelerate metal corrosion.

8.2.2.2 Sensors

One of graphene's most visible and useful applications is as an active element in sensing platforms. Electrochemical sensors can be constructed from graphene or rGO with excellent sensitivity, selectivity, reproducibility and a high dynamic range [41]. rGO is a good platform due to its high electrical conductivity, and the ability to chemically functionalize the oxygen moieties on rGO to include DNA, enzymes, cyclodextrins, supramolecular complexation agents, etc. as sensing elements [43, 52, 53]. Graphene itself can act as a sensing element, using the effect of analyte adsorption on the electronic properties of the sheet [54]. This field has been extensively reviewed [55–58]. The broadband absorption of graphene can be exploited in photodetectors utilizing the photovoltaic, photo-thermoelectric and thermal bolometeric effects [16, 59]. The advantage of graphene is the wide operating wavelength range, and its fast response time.

8.2.2.3 Energy Storage and Production

Graphene's unique combination of electrical, optical, and physical properties makes it an attractive material for several energy storage and production applications. This has been extensively reviewed by Brownson *et al.* [60, 61]. Graphene-based electrodes have been shown to improve the cyclic performance and energy capacity of Li-ion batteries due to their higher surface area, improved intercalation capacity, and rapid diffusion [56, 60, 62–64]. A new class of graphene-based supercapacitors is set to make a significant contribution to energy storage technology [13, 14, 65–69]. These supercapacitors combine the energy storage capacity of batteries (~0.1 W h cm^{-3}) with the power density of capacitors (~10 W cm^{-3}). The highest performing of these are based on electrodes of LrGO [14, 66] due to (i) its high porosity and surface area which allows for greater charge accumulation, (ii) its 2D-like structure which allows for rapid ion diffusion andfast charge/discharge rates, and (iii) the high electrical conductivity of graphene which gives low energy loss and discharge time constants as short as 20 ms [13].

8.2.2.4 Biomedical Technologies

The use of graphene in the field of biomedical technologies is still in an early stage, but progress is accelerating. Due to its extremely high surface area, graphene has attracted interest as a drug/gene delivery vehicle. This often utilizes π–π stacking interactions (for delivering drugs with aromatic groups), or the overall negative charge of GO, which allows electrostatic interactions with hydrophilic (positively charged) compounds [43]. Functionalization of GO with folic acid (FA) has been demonstrated in order to target drugs to FA-receptor cancer cells [43]. However, the use of LrGO in biomedical applications is still in its infancy.

8.2.2.5 Electronic Devices

Unsurprisingly, graphene is a promising material for a plethora of electronic technologies, and is the subject of several recent review articles on the subject [61, 70]. Its high carrier

mobilities and ability to engineer a bandgap via doping or strain makes it useful for transistors [61, 71, 72]. Furthermore, mechanical flexibility, non-toxicity, and relative transparency also make it well suited to applications such as wearable electronics [73, 74], touch-screen displays [16], conducting inks, and electronic paper [75].

8.2.2.6 Photonics and Optoelectronics

Graphene and rGO have been used as saturable absorbers in ultrafast fiber lasers [76], achieving wideband tunable modelocking to yield picosecond and sub-picosecond infrared pulses [18, 77–79, 80, 81]. The light emitting properties of graphene-based materials can also be used in LEDs [82] or more commonly, in imaging and fluorescent labeling of biological systems [29, 43, 53, 83]. Graphene displays a higher biocompatibility than some toxic fluorescent dyes, and can be functionalized to target specific analytes [84] (e.g. proteins, DNA, cell membranes). This has been employed successfully as FRET [85] and fluorescence quenching sensors [86].

8.2.3 Synthesis of Graphene—An Overview

There are many methods available for the synthesis of graphene materials, summarized in Figure 8.3 below. Laser reduction of GO is judged to result in a lower quality graphene material than does CVD and mechanical type exfoliations, on par with graphene materials made by liquid phase exfoliation. Due to the high capital cost of lasers and energy requirements, we estimate that the cost for mass production will be higher than liquid phase exfoliations. However, the advantages of *in situ* patterning and quick fabrication of rGO devices easily make up for the higher cost. Indeed, using laser photoreduction as a tool for quick prototyping of

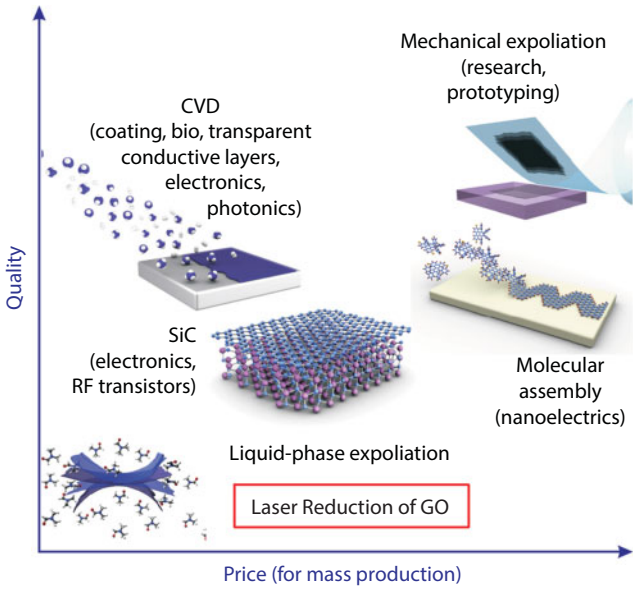

Figure 8.3 Methods of synthesis of graphene materials classified based on price vs. quality. Copyright Nature 2012. Reproduced with permission from Ref [75].

devices is highly attractive. In this section, we discuss the other major approaches to manufacturing graphene, to set the stage for comparisons with laser reduction.

8.2.3.1 Chemical Vapor Deposition

Chemical vapor deposition (CVD) is one of the most important methods for production of graphene, in spite of its higher complexity, due to its ability to form high quality, defect-free graphene and ability to tune the graphene's properties. Typical CVD processes involve a metallic substrate (most commonly Ni or Cu) annealed at high temperature, and a mixture of H_2/CH_4 gas which subsequently reacts or decomposes onto the substrate to form the graphene [87]. Current challenges involve growing graphene with large, controlled grain sizes, growing directly onto insulating substrates, finely controlling the number of layers, and using cost-reducing lower temperature growth processes [87].

8.2.3.2 Pulsed Laser Deposition

Similarly to CVD, pulsed laser deposition (PLD) exposes a substrate to a carbon-containing vapor, which in this case is generated by ablating a carbon target with a pulsed laser [88]. PLD has a number of advantages over CVD, mainly that high-quality graphene can be deposited on insulating substrates as well—PLD of graphene has been demonstrated on silicon and fused silica [89, 90]. The main drawback of PLD compared with CVD is its limited ability to deposit graphene onto intricate 3D substrate geometries. The graphene grains produced by this methods are also of relatively small size (several tens of nm [91]), limiting their application in areas where large grains of graphene are required.

8.2.3.3 Exfoliation

Since the first reported fabrication of graphene in 2004, exfoliation has been a key method for producing single-layer graphene [1]. It relies on overcoming the weak van der Waals attraction between graphene layers by mechanical force to peel off subsequent flakes of graphene from bulk graphite. Such methods are however quite labor intensive and difficult to carry out at scale. Recently, liquid phase exfoliation methods have emerged which are readily scalable, with production quantities reaching up to 73 mg/h [92]. These include sonication [93], electrochemical methods [94], ball milling [92], or shear mixing [95]. The process can be assisted by the presence of ions that intercalate the layers or by surfactant molecules [96, 97] to help disperse the exfoliated sheets and prevent aggregation. Sonication relies on normal forces and has a low graphene yield, but produces relatively defect free and pristine layers [98]. By contrast, ball milling uses shear forces to separate the layers, and is faster with higher yield, however the fragmentation caused by the high energy process means that only small flakes are obtained [99]. Shear mixing uses fluid flow to create high shear forces to exfoliate the graphene sheets, however these can suffer from similar cavitation issues as sonication methods, introducing unwanted defects [99].

8.2.3.4 Graphene Oxide/Precursor Reduction

The conversion of graphite to graphite oxide and then back to rGO may initially seem like a counter-intuitive process, but has been hugely successful [100]. The conversion of graphite

to graphite oxide is usually performed by the modified Hummer's process, and will be extensively reviewed later in the chapter. Upon reduction, islands/grains of conjugated graphene structure are restored, which results in a higher conductivity and enables rGO to approximate many of the prized properties of pristine graphene. Hence, the reduction of GO has emerged as the preeminent way to produce graphene for applications in electrochemistry, sensing, and photocatalysis. While GO reduction often produces graphene with a higher concentration of defects than with other methods, these defects can often be useful. The key consideration is the heterogeneity of the oxidation functionalities produced, and the difficulty in characterizing the exact nanoscale structure of graphite oxide. This heterogeneity in the type of graphene produced is characteristic of different reduction methods used, and indeed can vary even within the same method. The structural and functional properties of GO and rGO will be discussed in Section 8.4 below.

Chemical reduction of GO involves treatment with reducing agents that cleave the carbon–oxygen bonds and restores the planar, sp^2 conjugated graphene structure. Reagents used include hydrazine monohydrate, hydroiodic acid, and sodium borohydride [100, 101]. Thermal annealing can also be used subsequently or simultaneously (solvothermal reactions [102]) with chemical reduction to increase electrical conductivity. Compared to other methods, the defect density of chemically reduced GO is substantial, to the order of magnitude of 0.01% [56, 103].

Electrochemical reduction can be achieved by direct electron transfer from an electrode to GO layers in solution or deposited on the electrode. Regular electrochemical cells have reduction (electron donation) at the cathode and this process does not require added reagents, but is sensitive to factors like pH and temperature [104]. The electrochemical reduction is irreversible, easy to perform, and can yield films with a conductivity up to 85 S/cm [105], which is comparable to chemical reduction with hydrazine (up to 99.6 S/cm [106]). This can be improved up to 350 S/cm at a high negative applied potential [107].

Thermal reduction of GO removes carbon–oxygen functionalities as CO_2 and CO gas, and the resulting rGO is usually highly defective (containing basal plane vacancies), of small grain size, and can have an exfoliated and wrinkled structure. Exfoliation occurs due to the rapid expansion of gases released by the heating process. Thermal treatment can be performed in a traditional furnace (from ~500 to >1000°C) or hydrothermally [108]. While thermal reduction is facile, the energy cost for heating can be high, and the resulting rGO has a lower conductivity compared to other reduction methods. In addition, the temperature required for reduction can often degrade the substrate upon which GO is deposited.

Photoreduction combines the advantages of thermal and chemical reduction with the ability of a light source to selectively draw patterns and fine features. This approach is the focus of the rest of this chapter: the photoreduction of GO to rGO. Furthermore, photoreduction obeys the principles of green chemical synthesis as it does not require the use of harsh reagents. The main limiting factor for photoreduction techniques is the true scalability of the technology (*i.e.*, the throughput and synthetic yield). However, this is not a limitation for most of the main applications of photoreduced GO, such as in electrochemical capacitors and sensors. Parallel processing using spatial light modulators or fast galvo-scanners holds the potential to increase the speed and hence throughput of laser rGO production.

8.3 Overview of Laser Reduction of GO to rGO

8.3.1 Photoreduction of GO

In this section, we review the main techniques used to perform the reduction of GO, with different sources of light. We do not aim to be exhaustive, and instead summarize representative papers in the field that demonstrate the main characteristics of each technique, and the associated advantages/disadvantages. The different photoreduction methods are classified based on whether they employ the use of coherent light or not, and by the nature (continuous wave, pulsed and pulse duration) of the radiation sources used to induce the reduction process. This classification becomes useful as an organizing tool in distinguishing between different atomistic mechanisms of the photoreduction process.

8.3.1.1 Incoherent Radiation Reduction of GO

Coherent radiation, *i.e.*, laser radiation, is a popular tool for photoreduction, however successful photoreduction has also been demonstrated using incoherent radiation. The most notable example of this is the use of microwave radiation, first demonstrated by Zhu *et al.* using a common kitchen microwave [109]. Microwave radiation is absorbed and generates a plasma, producing a local high-energy environment where graphite oxide is chemically reduced and exfoliated. Further work has shown that this process can be made faster, and the quality of rGO improved, by using pulsed microwave radiation and adding a small amount of graphite powder to catalyze the reaction [110, 111].

Microwave reduction of GO is an attractive method for larger-scale production, as it is fast and scalable, and allows the reduction and exfoliation steps to be carried out simultaneously. Molecular dynamics simulations indicate that the fast heating caused by microwave radiation allows oxygen-containing moieties to be removed at a timescale too fast to undermine the stability of the graphene sheet, resulting in reasonably high quality rGO [112].

In addition to microwave radiation, photoreduction of GO by ultraviolet (UV) and by infrared (IR) lamps has also been reported. Reduction of GO by IR light is thought to occur by a photothermal mechanism, where heating of the GO by light absorption drives the reduction process [113]. A similar photothermal process can also be used to reduce GO using heating produced by UV light, however catalysts can also be used with UV light to produce rGO by a photocatalytic reaction rather than a photothermal route [114].

8.3.1.2 Continuous Wave Laser Reduction of GO

Continuous wave (CW) lasers are the most widely used tools to produce laser reduced GO (LrGO), due to the availability and low cost of CW lasers and associated optical elements. Furthermore, the quality of rGO produced is often very high, with a large I_{2D}/I_G ratio and small I_D/I_G ratio in the Raman spectra and high conductivity. In CW laser treatments, the parameters that are often varied in device optimization are the laser wavelength, laser power, laser spot size, and scan speed. The last three parameters control the overall laser fluence, or energy deposited per unit area, which is the true control parameter.

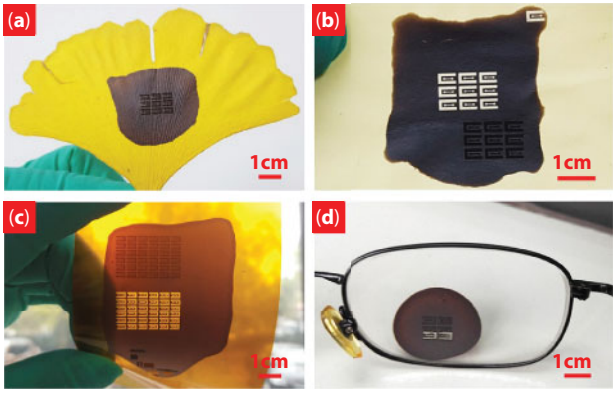

Figure 8.4 Deposition of GO on various substrates (a) Gingko leaf, (b) sticky note, (c) polyimide film, and (d) glass lens and subsequent continuous wave laser reduction of GO. Reproduced with permission from [119]. Copyright 2016 Elsevier.

Complex patterns can be directly written onto onto a variety of surfaces (Figure 8.4) using traditional galvo-scanner or stage translation methods, or using holographic techniques based on spatial light modulators [115].

The reduction mechanism is mainly photothermal in nature, as the continuous wave lasers deposit energy into the GO system in a manner that is often wavelength independent and creates rGO solely due to the high temperatures reached at the focus of the laser. This is because GO has an absorption spectrum that lacks any peaks in the range of typical CW lasers used, and no nonlinear absorption processes dominate for CW lasers with low intensities. The ability of CW lasers to deliver more overall energy however reinforces the photothermal reduction effect relative to pulsed lasers that have a high peak intensity with small pulse energy (~1–100 mJ). Photothermal reduction also results in a more exfoliated graphene sheet structure, and hence a greater surface area and density of electrochemically active edges. As with all laser treatment methods however, a transition between laser reduction and laser ablation is often observed, as the laser power increases or the overall dose/energy deposited increases [116]. However, the onset of laser ablation and oxidation can be suppressed by laser treatment under an inert nitrogen atmosphere [117], and a more pristine graphene structure synthesized [118].

Pioneering experiments in the CW laser treatment of GO was performed by the group of Kaner *et al.* [120, 121] in UCLA. By simply using a CW laser contained within a LightScribe DVD drive (788 nm), they demonstrated the ability to tune the conductivity of rGO over five orders of magnitude by changing the write-speed and power of the laser. This method was used to pattern electrochemical gas sensors, electrodes, and supercapacitors. The supercapacitors fabricated had specific capacitances up to 5 $mFcm^{-2}$ and retained their stability over many bending cycles, with excellent charge/discharge rates [13, 121]. Using a simple LightScribe DVD drive afforded ease of patterning, as a commercial DVD label burner software could be used to create the patterns required, and the GO was simply deposited onto a PET film and subsequently adhered onto the surface of the DVD disc. The LightScribe method produces rGO that is comparable to nanosecond pulsed laser synthesized rGO when characterized with Raman spectroscopy (high 2D band) and XPS (high C:O ratio) [122]. Others have also adapted different CW lasers to

produce planar supercapacitors [123, 124], and even fiber supercapacitors, with capacitances up to 1.2 $mFcm^{-2}$ [125, 126]. A disadvantage of CW (LightScribe) LrGO is the poor adherence of LrGO on a substrate under aqueous solutions, due to the solubility of remnant GO from incomplete photoreduction. This can be alleviated by casting an initial blend of GO and PVDF-HFP [127] prior to LightScribe laser reduction, to increase the water wear resistance, without compromising the electrochemical activity.

Although laser photoreduction of GO is a natural choice for reduction of solid films, it is not limited to this configuration, and lasers can also be used to reduce GO suspended in solution. If this occurs in the presence of another reducible reagent, the other reduction product can decorate the surface of the resulting rGO sheets. This has been used to create Ag and Au decorated rGO sheets for surface enhanced Raman spectroscopy, using reduction of GO in the presence of $AgNO_3$ [128] or $HAuCl_4$ [129]. Furthermore, this strategy was used to dope graphene with fluorine, by irradiating a fluoropolymer covered graphene precursor with a 488 nm CW laser, to create highly insulating structure [130]. The effect that GO reduction has on adjacent structures can also be seen in lipid vesicle deformation around GO aggregates due to the release of gases upon CW laser reduction [131].

While an increased degree of graphenization is preferred during the reduction process, sometimes the graphenization degree measured by Raman spectroscopy does not necessarily correspond to the highest conductivity [132], due to the effect of the sample changing during characterization as the Raman spectra were acquired, or to the existence of internal networks of graphene (in thick samples), that are not probed in the focal volume of the Raman laser. In most cases however, for sufficiently thin rGO (few microns), a high I_{2D}/I_G ratio often corresponds to a higher conductivity [133].

Due to the intimate relationship between defects and the electronic properties of CW laser rGO, a detailed investigation into the effect of defects and domain sizes on the electrical resistivity was performed, and an inverse relationship between the Raman I_D/I_G ratio and resistivity found [134]. This runs counter to usual expectations for monolayer graphene, because the multilayer rGO produced had a higher density of small sp^2 domains [135] for charge to percolate. This indicates that CW lasers in solid-state reduction and ambient conditions are not very capable of healing defects and increasing the overall sizes of sp^2 domains. This is corroborated by the study of Eigler *et al.* which shows an increase of the I_D/I_G ratio up to 2.8 upon laser reduction [136]. Instead, the route to more conductive graphene samples must be in the deoxygenation of larger GO sheets into smaller sp^2 domains, allowing charge to percolate through them and increase conductivity.

Using a CW laser, groups have also demonstrated the ability to manipulate the optical properties and the surface wetting properties of rGO surfaces. Furio *et al.* [134] used a CO_2 laser (10.6 μm) and UV lamp to fabricate rGO surfaces, and tune the water contact angle from 22 to 105°. The CO_2 laser afforded a more conductive rGO film than a LightScribe laser. Furthermore, the broadband (450–800 nm) linear transmittance could be tuned over two orders of magnitude using different UV lamp exposure times. A positive relationship between contact angle and conductivity was observed, due to the increased graphenization and removal of oxygen groups simultaneously increasing the hydrophobicity and conductivity. CO_2 lasers have proven versatility in reduction of GO, and have even been shown to be able to create porous graphene from laser treatment of wood [137]. Optoelectronic devices made of rGO such as fiber Bragg gratings [138], thermal bolometers [139], rGO–Si heterojunction photodetectors [119] have also been

fabricated with CW laser reduction. Using the florescence quenching that occurs due to transformation from GO to rGO, fluorescent "barcodes" can be written onto GO deposited onto surfaces [140].

CW LrGO has been applied as a strain gauge (measuring change in resistance as a function of applied strain) [141]. Further sensing capabilities, such as mechanical deformation in response to ambient humidity has been leveraged to create walking robots and humidity responsive textiles, via fabrication of a GO–rGO layered composite [126].

8.3.1.3 Nanosecond Pulsed Laser Reduction of GO

Nanosecond lasers are another prominent class of pulsed lasers used to produce rGO. The quality of rGO produced by nanosecond lasers (as measured by the Raman I_{2D}/I_G ratio, conductivity, and density of defects) is the highest among the pulsed lasers. For pulsed lasers, the main parameters that can be optimized are the laser wavelength, repetition rate, pulse duration, laser fluence, focusing lens numerical aperture, and number of overlapped pulses (or scan speed). All these factors change the amount and distribution of energy deposited in 3D space, and the rate of the energy deposition.

Nanosecond lasers have a pulse duration of single digit to tens of nanoseconds. During this pulse, there is ample time for thermal effects to accumulate and deoxygenate GO. Many nanosecond pulsed lasers operate in the UV region (e.g. excimer or frequency doubled/tripled YAG lasers), and hence induce photochemical effects in addition to photothermal effects. GO has an absorption spectrum that peaks at around 200–300 nm. Hence, GO will absorb UV light and undergo well-known photochemical reactions (e.g. Norrish type reactions at carbonyl centers [142]) that involve free radicals. There is also the generation of a plasma plume, which can cause re-deposition of material around the laser treated zone, and ablation that occurs concomitant with laser reduction. Some of the first examples of pulsed nanosecond laser (248 nm, 355 nm, 532 nm) reduction of GO was performed in the solid state by the in 2010 (Figure 8.5), and yielded the characteristic heterogeneous structure of the nanosecond laser treated zone, with pristine 2D layers in the centre but more disordered regions on the edges [118, 143]. Future works often performed rastering of the laser during reduction, to make the surface more homogeneous. Arul *et. al*. performed an optimization of the fluence and number of overlapped pulses (Figure 8.5) in order to determined the optimum parameters to produce pristine graphene with clear 2D Raman band signatures [122]. The quality of the laser treatment can be increased by laser irradiation under an inert gas, vacuum, or hydrogen gas atmosphere. Hydrogen gas atmospheres have been shown to increase the final rGO conductivity achieved [144], however the difference compared with reduction in ambient conditions is small [145, 146]. More generally, nanosecond pulsed lasers can also be used to manipulate the nanostructure of GO materials by laser ablation in addition to reduction. Lin *et al.* have synthesized a variety of one-dimensional GO nanostructures (nano-squares, nano-triangles, nano-hexagons, etc.), which exhibit tunable photoluminescence [147].

The sheet resistances of nanosecond LrGO are very low (~100–500 Ω/sq [143]), beating other pulsed laser reduction methods by a decent margin. However, continuous wave laser reduction often performs better, resulting in rGO with a lower resistance (<80 Ω/sq [13, 66]) than nanosecond laser reduction, however a recent study of picosecond laser reduction

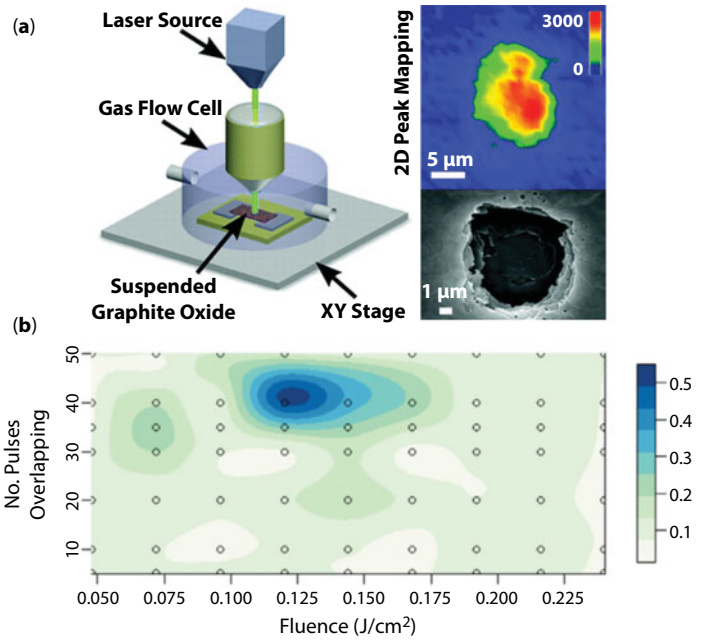

Figure 8.5 (a) Schematic of the laser reduction equipment used and the resulting reduced graphene oxide with the 2D Raman peak chemically mapped across the surface. Reproduced with permission from [118]. Copyright 2010 American Chemical Society. (b) Heat map of quality of nanosecond LrGO fabricated, as measured by the Raman I_{2D}/I_G ratio, when the laser fluence and number of pulses is varied. Reproduced with permission from [122]. Copyright 2010 American Chemical Society.

(10 ps, 1064 nm, 100 kHz repetition rate) of GO under liquid nitrogen yielded high quality rGO with sheet resistances as low as 50–60 Ω/sq [148]. Nanosecond lasers can also be used to coat GO and rGO onto various substrates using pulsed laser deposition. This has proven useful in the integration of rGO onto different wafer substrates commonly used in the semiconductor industry (e.g. Cu, TiN, and Si [149]).

Nanosecond laser reduction of GO in aqueous solutions was performed by Huang *et al.* [150] and Abdelsayed *et al.* [151] in 2010, to yield dispersed rGO sheets that can be subsequently cast onto films. Later work explored the solution-based nanosecond laser reduction of GO further [152, 153]. Aqueous nanosecond pulsed laser reduction can also be performed in ammonia solution [154] yielding results comparable to chemical based reduction methods with hydrazine, although the rGO produced did not have a very high conductivity, high I_{2D}/I_G ratio, or high C:O ratio. Most laser treatments were performed with the harmonics from a Nd:YAG pulsed laser at a low repetition rate (~10Hz) and with pulse durations on the order of several ns (~5 ns) [155, 156]. As with CW laser treatments, aqueous reductions are affected by reagents in the surrounding solution, and the reduction process can be assisted by reducing agents that are activated by irradiation. An example is the reduction of GO assisted by the photocatalytic activity of polyoxometalate clusters, to yield rGO with an enhanced saturable absorption characteristic [157]. Silver and nickel nanoparticles can also be deposited on rGO via *in situ* photoreduction of the precursor metal salts [158]. Solution based nanosecond laser treatment has been implemented in several unique applications, such as in photocatalysts and sorbent materials. Russo *et al.* synthesized aqueous rGO to

create a material that can adsorb pollutant dyes [159]. Dye removal can also be performed by reduction of rGO in the presence of TiO_2 to create nanostructures of TiO_2 nanoparticles supported by sheets of rGO [160] and operates as a good visible light driven photocatalyst for water splitting [161].

Rather than aqueous solutions, GO can also be dispersed in a frozen matrix of water or other solvent and deposited onto a surface by pulsed laser deposition. This technique is known as Matrix Assisted Pulsed Laser Evaporation (MAPLE), and has been used to simultaneously deposit and reduce GO to rGO onto quartz/silicon substrates [162–164].

By laser scribing structural gratings onto the surface of GO, two-beam laser interference can induce super-hydrophobicity to rGO–GO structures with contact angles up to 157° [165, 166]. This is attributed to chemical changes (increase in sp^2 graphene domains and reduction in hydrophilic oxygen groups), and structural changes (Cassie impregnated wetting). These super-hydrophobic gratings also display optical iridescence.

Doping of rGO during the photoreduction process can be accomplished by flowing a gas (Cl_2 or NH_3 [167]) on the surface of GO or deposition of GO on a dopant containing substrate such as GaN [168]. Conversion of rGO from p to n-type can be done purely by changing excimer laser processing conditions and changing the extent of reduction of the rGO [169].

Supercapacitors, while more commonly synthesized with a CW laser, can also be made with nanosecond and picosecond pulsed lasers. Picosecond pulsed lasers can fabricate supercapacitors made of porous rGO, but with capacitances of ~38 $mFcm^{-2}$, which is smaller than the equivalent CW laser scribed versions [170]. With nanosecond excimer laser treatment, the capacitances are even lower, with a maximum of 2.4 μFcm^{-2} achieved [171].

Nanosecond LrGO has also been used in various sensing applications such as photodetectors and rGO-paper based electrochemical sensors [172]. Bolometers of rGO with 90–98% absorption of light in the visible to IR range has been used to construct a photodetector with a high sensitivity and thermal coefficient of resistance [173]. While thick rGO films absorb light well, thinner rGO films can act as transparent electrodes for photovoltaic applications, combining high conductivity and high optical transparency. Konios *et al.* constructed flexible organic photovoltaic cells containing rGO electrodes with 3.05% power conversion efficiency, and is the most efficient solar cell reported of its kind [174].

8.3.1.4 Femtosecond Pulsed Laser Reduction of GO

Femtosecond lasers are a high-tech tool that are only recently moving from optical research into applications in industrial materials processing. They use an ultrashort laser pulse on the order of 100 fs (100×10^{-15} s), usually centered in the infrared region of the spectrum (800–1030 nm). These lasers are often used for micron-scale material removal (ablation), where the ultrashort pulse duration allows the material to be ionized and ejected before there is significant heat transfer to the atomic lattice (*i.e.*, the pulse duration is shorter than the electron–phonon coupling time—typically picoseconds), enabling laser micromachining with little or no heat affected zones.

A common phenomenon in femtosecond laser ablation is the incubation effect – where the energy required for material removal lowers as a result of photoinduced defect

accumulation in the material. Recent work has observed this effect in GO and highly oriented pyrolytic graphite, however rGO was not seen to display this effect, which is thought to be a result of the defect-rich structure of rGO films and their ultrafast energy relaxation [175].

Reduction of GO films using femtosecond pulsed lasers was first demonstrated in 2010 by Zhang *et al.*, who demonstrated ability to tune the resistivity of the rGO by varying the laser power [176]. Although there are numerous experimental parameters that can be modified during femtosecond laser reduction of GO, the resulting rGO materials typically share similar characteristics. The brown GO film gradually turns black upon reduction, detailed in the UV-Vis absorption spectra, where a red-shift and overall increase in absorption is seen. Reductions in layer thickness and spacing are also observed (by XRD and AFM). XPS is perhaps the most commonly used method to measure reduction of femtosecond laser rGO, where loss of C–O binding groups in the C 1s spectra and higher C:O elemental ratio are clear indicators of reduction [177].

Despite these indicators of reduction that femtosecond laser rGO shares with other rGO, there are some critical differences that arise as a result of the ultrashort pulse duration used. Femtosecond laser reduction results in removal of oxygen-containing moieties (with higher energy bonds being preferentially removed), as evidenced by XPS spectra, however the ultrashort pulse duration means that in most cases insufficient heat is transferred to the graphene lattice to drive the sp^3–sp^2 structural rearrangement [122]. The presence of the rearranged sp^2 structure is confirmed by the Raman 2D band at around 2700 cm^{-1} [118, 178], which is often not prominent in femtosecond laser rGO due to the non-thermal nature of the process. By raising the pulse energy, number of pulses, or pulse repetition rate however, lattice heating and incubation can result in the sp^3–sp^2 structural rearrangement [179, 180].

In addition to ablation and reduction, it has been demonstrated that femtosecond laser processing can achieve simultaneous reduction and doping of GO with nitrogen, using an ammonia atmosphere [181]. By tuning the laser power, the N-doping concentration and the bond type (pyridinic or pyrrolic) can be adjusted, allowing the fabrication of graphene-base field effect transistors. Reduction of GO by femtosecond laser pulses has been shown in aqueous GO solutions as well, where it provides a simple and non-toxic alternative to the more common chemical reduction process used to prepare aqueous rGO for applications such as supercapacitors and electroanalysis [177].

Due to the ability of femtosecond pulsed lasers to carry out precise micron-scale patterning without thermal damage to the surrounding area, femtosecond laser rGO has found applications in various optical and optoelectronic devices. It has been used as an electrode in organic photovoltaic cells and organic light-emitting devices, where the high conductivity and optical transparency (for few GO and rGO layers) are essential [179, 182]. The change in refractive index of GO upon reduction to rGO by femtosecond laser pulses has also been exploited in the production of holograms for data recording and wavefront shaping. The fine control over the reduction reaction afforded by femtosecond laser pulses allows gradual reduction and adjustment of the refractive index of rGO in a way that can be spatially patterned, enabling fabrication of ultrathin optical lenses [183]. This refractive index modification also makes possible production of three-dimensional color holographic images with wide viewing angle, using the athermal production of rGO with spectrally flat refractive index modulation [28, 184].

8.3.1.5 Advantages and Disadvantages of the Laser Reduction Methods

The different laser reduction platforms allow for the synthesis of LrGO at different spatial resolutions, quality, and speed. Here we briefly review each platform and list its advantages and disadvantages.

CW laser reduction utilizes relatively inexpensive lasers (e.g. LightScribe DVD burners [121]), that can produce large areas of LrGO very quickly. Hence, it is the best candidate for large scale production of LrGO for application such as electrochemical supercapacitors and sensors. The disadvantage of CW laser synthesis is the limit of its resolution, with nanosecond and femtosecond pulsed lasers being able to pattern finer features with greater spatial control. There are a number of factors contributing to the reduced resolution. Firstly, the fundamental diffraction limit, which is higher for CW lasers that operate in the visible and IR compared to pulsed excimer lasers in the UV. Secondly, femtosecond pulsed lasers operate in a highly nonlinear regime, which results in a smaller laser affected zone because of nonlinear focusing and multiphoton absorption, whereas most CW lasers operate in the linear regime. Finally, photothermal effects widen the laser treated zone due to heat diffusion.

Nanosecond lasers have the advantage of a smaller fundamental patterning resolution, due to the diffraction limit of a UV wavelength pulse. Furthermore, as the heat deposition is more spatially localized and temporally short, the thermal diffusion away from the laser spot is minimized compared to CW lasers. The disadvantage of the method is the heterogeneity of the single shot laser treated areas, the laser induced ablation that can occur simultaneously with reduction [122, 143], and the often lower quality of rGO compared to CW lasers [118]. This lower quality manifests as wider FWHM of peaks in the Raman spectra, and in a lower I_{2D}/I_G and higher I_D/I_G. However, when just laser treating under ambient conditions, the two methods are comparable [122].

Femtosecond laser treatments promise very fine laser patterning of LrGO, however the requirement for high repetition rates and the higher cost of femtosecond lasers can often offset the perceived advantages. While femtosecond lasers are the tool of choice for precise micromachining of virtually any material [185], we believe that nanosecond and CW lasers are better suited for large-scale laser reduction of GO.

8.4 Mechanistic Understanding: Laser Reduction and Patterning of GO

The mechanism of the laser reduction of GO is still largely unknown. By drawing upon several studies, we attempt to build a picture of the timescales and fundamental chemical phenomena occurring during and after the laser irradiation process. As no time resolved, *in situ* state probe of the reduction process in the solid state has yet been performed, information about the elementary reaction steps must be deduced from analogous studies in liquid reduction or from computational simulations.

8.4.1 Photophysics and Photochemistry of Graphene Oxide Reduction

The overall reduction process depends on factors such as the energy deposited, the timescale of the reduction process, and the structure of the GO (chemical composition, intercalated

water, sheet morphology). Our hypothesis for the laser reduction mechanism proceeds as follows: GO laser reduction occurs via a two-step process [122]. The first step involves the photochemical removal of oxygen from the surface of GO. The exact mechanism of this step differs depending on the laser wavelength used, the pulse duration, and is often accompanied by laser-induced material removal/ablation. The second step is the structural reorganization of the carbon-based lattice into planar, sp^2 conjugated domains. This step is mediated by thermal effects, and can be spatially heterogeneous in nature depending on factors such as the laser's spatial intensity profile, treatment conditions, anisotropic thermal diffusion, etc. These two steps occur on different timescales. Photochemical reactions can be induced within a few hundred femtoseconds, while the earliest step of thermal diffusion (the transfer of energy from the electrons to phonons/molecular vibrations) occurs on the order of tens of picoseconds.

8.4.1.1 Photochemical Reduction

The photochemical reactions that occur during the laser reduction process can be classified into two separate regimes, those due to linear absorption and those due to nonlinear absorption effects. Nonlinear absorption effects only occur in the regime of high intensities within picosecond and sub-picosecond pulsed laser interactions, while linear absorption dominates for nanosecond and continuous wave lasers. Optical bandgaps are hard to estimate, as GO is a heterogeneous material. To the extent that we can treat GO sheets as semiconducting, Liaros *et al.* propose a ~0.6 eV gap corresponding to non-oxidized sp^2 and sp^3 regions, and a further 2.6–3 eV gap from the oxygenated regions [186].

Depending on the chemical functionalities present on the surface of GO, different processes can occur that lead to reduction. Overall, it has been determined that the structure of GO most closely follows the Lerf–Klinowski model [187, 188], where the basal-plane functionalities are epoxides and hydroxyls, with carboxyls, carbonyls, and lactones at the edges [189]. This is supplemented by small domains of graphitic sp^2 regions, which are present due to incomplete oxidation. Further studies have also shown the presence of humic and fulvic acid like debris of <50 nm in size that decorate the surface of the larger GO sheets, when GO is synthesized via the Hummers–Offerman method [190]. This can be seen in Figure 8.6 below, where the differences between graphene, GO, and rGO are depicted.

The study of the complex mechanisms occurring during GO photoreduction has been hampered by the lack of uniformity and the structural complexity of GO itself. Recent work by Hong *et al.* has attempted to elucidate the effect of different functional groups on the reduction of GO, using two-photon oxidation of graphene to carefully control the functional groups present [192, 193]. Hong *et al.* found that laser reduction can cause redox reactions that convert one functional group to another, over a timescale of tens of seconds. This finding has an impact on both photothermal [194] and photochemical reduction [195]; when the total C:O ratio is high, reduction occurs by epoxide diffusion and subsequent removal, whilst high binding energy functional groups (like carbonyls and carboxyls) are first converted to lower binding energy groups (like epoxides or ethers) prior to full reduction. If the C:O ratio is low, redox reactions that convert epoxides and ethers to carboxyls and carbonyls occurs first, then a stepwise reduction to sp^2 and residual sp^3 carbons.

We can also examine analogous photodisassociation reactions of small carbon-based fragments, extensively studied in the molecular photochemistry field, to understand the

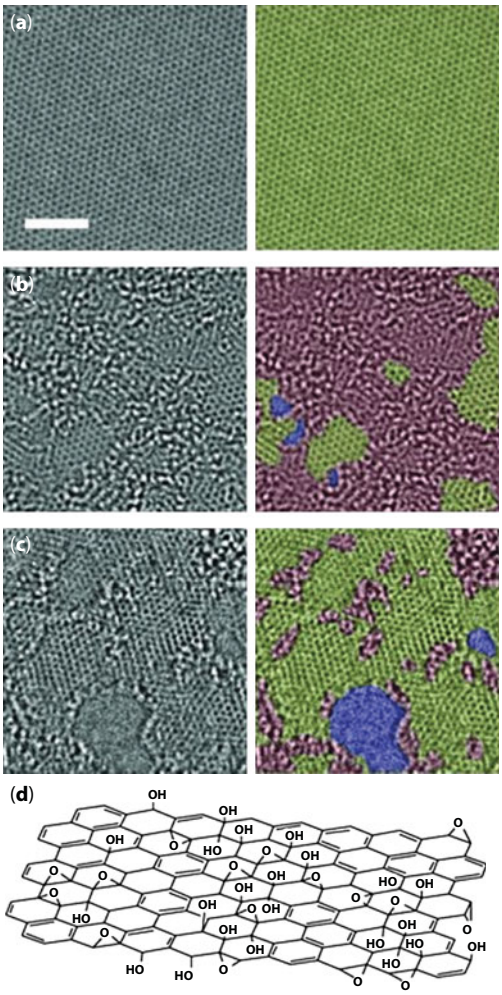

Figure 8.6 Aberration corrected TEM images of (a) Pristine graphene. (b) GO with holes (blue), graphitic domains (yellow), and oxygenated domains (red). (c) rGO with holes (blue), graphitic domains (yellow), and oxygenated domains (red). Copyright 2010 Wiley. Reproduced from [191] with permissions. (d) Schematic of the Lerf–Klinowski model of GO. Copyright 2009 Royal Society of Chemistry. Reproduced from [142] with permissions.

photoreduction of GO. Plotnikov *et al.* have performed a detailed analysis of the possible reaction mechanisms involved in the disassociation of small molecules from GO, and the expansion of sp^2 domains under incoherent UV radiation [196], which was also observed by Matsumoto *et al.* [197]. GO absorbs light primarily in the UV region, at ~227 nm. As effective photoreduction progresses, the absorption maximum redshifts to ~265 nm, which indicates an increased size of sp^2 conjugated domains [9]. Signatures of increased conjugation and removal of oxygenated groups could also be observed in the fluorescent excitation–emission maps [198]. The growth of sp^2 conjugated domains was attributed to the migration of remnant epoxide and hydroxyl fragments to the periphery of sheets, which is estimated to have an energy barrier of ~0.9 eV and hence easily surmounted by light sources with wavelengths shorter than ~1378 nm. Indeed, this hydroxyl migration step has

been observed via *in situ* photoluminescence studies during the reduction of a single GO flake under 405 nm continuous wave irradiation [199].

The disassociation of CO, CO_2, H_2O, and O_2 molecules is also expected to occur from an electronically excited state, rather than from a vibrationally excited ground state. This underscores the main difference between traditional photochemical and photothermal reductions. Photothermal reductions involve a vibrationally excited ground state, which are populated either via heating or by relaxation from an electronically excited state. Photochemical reduction occurs from the excited state and has a dependence on the spin multiplicity (singlet/triplet) of the states involved.

The R–O, and O–H fragments (where R represents an all-carbon fragment) have excited states that are repulsive (anti-bonding) with triplet and singlet characteristics, hence excitation into either state will result in bond cleavage. However, the triplet excited states are higher in energy [196, 200], and unlikely to be populated by a single UV photon. The excited state for the C–O singlet is lower in energy than the O–H singlet [201], hence the C–O bond will be preferentially broken. Similar considerations occur for the elimination of CO and CO_2 from carboxyl (RCO_2H) and carbonyl (RCHO) functionalities [202]. The elimination of these groups occurs in a concerted reaction with simultaneous hydrogen transfer to the remaining carbon fragment. The removal/photolysis of epoxy, carbonyl, and carboxyl functionalities can be tracked by a decrease in the absorption of GO, especially if the photolysis goes too far and degrades the structure of the resulting rGO [199]. However, the C–C bonds that comprise the main carbon network are not easily broken by purely photochemical means, as its disassociative triplet excited state is high in energy [203].

As discussed above, irradiation with UV photons causes photochemical reduction and photothermal reduction [197] and is required for linear absorption by GO sheets, both as films and in solution. Visible wavelengths are more weakly absorbed, but absorbances remain around 0.5 until ~400 nm for GO so that photochemical reduction with visible light is still possible. At continuous wave laser wavelengths of 532 and 635 nm, there is poor linear absorption and no photochemical reduction occurs. However, once infrared radiation is used, or at high laser powers, the mechanism changes from a photochemical to a photothermal one [194]. Any photochemical reactions would have to proceed via nonlinear absorption mechanisms, which become important under the extremely high photon flux from ultrafast lasers for example. In the ultrafast regime, photooxidation [193] is a competing mechanism with photoreduction. Photooxidation is detrimental to the reduction of GO to rGO, as it will reduce the C:O ratio and the size of the graphene-like domains.

The nonlinear response of GO has been extensively characterized by Zheng *et al.* [27]. They discovered four distinct regimes of nonlinear effects (such as saturable absorption, Kerr nonlinearities, etc.) as a function of the laser fluence for an 800 nm, 100 fs pulse laser, at a 1kHz repetition rate. The four regimes (ordered from low to high fluence regimes) are; (i) saturable absorption, (ii) two-photon absorption and excited state absorption of the sp^3 matrix, (iii) onset of reduction of GO, and (iv) completion of reduction of GO. Machining with fluences beyond the final regime results in laser ablation. However, the rGO produced with the higher fluence of regime (iv) does not have a significant 2D Raman band, despite evidence (from XPS) that oxygen is removed [184]. This indicates that there is no relaxation of rGO sheets to a planar graphene layer, with extended sp^2 conjugation.

Similar to the discussion of linear absorption photochemistry, there is also the influence of functional groups on the nonlinear absorption. Also, lower oxidation % or a higher sp^2 carbon content results in higher nonlinear absorption, a trend observed for femtosecond [27, 204] through to nanosecond laser reduction [156, 205]. Curiously, there is even a nonlinear absorption for continuous wave lasers at 405 nm, which decreases as GO is laser reduced (at that same wavelength). While wavelength dispersion of the nonlinear index and two-photon absorption cross-section is observed in rGO [206], generally as the sp^2 content increases, the nonlinearity also increases [207].

8.4.1.2 Photothermal Reduction

In order to understand the photothermal aspect of the laser reduction of GO, we turn to studies on the thermal reduction of GO as a guide. It is assumed that, at the microscopic level, there is a similarity between the structural change to GO induced by photothermal effects vs. purely thermal effects. There are differences in the morphology of the final product however, due to the rastering motion of the laser and the localized deposition of heat, compared to the more isotropic heating in furnace based thermal GO reduction.

Thermogravimetric studies have shown the presence of two separate steps of material removal/resorption during the reduction process. The first, occurring at ~150°C involves the removal of epoxide and hydroxyl functionalities, while another at 600°C is attributed to other functionalities like the edge carbonyl and carboxyls [187]. Synchrotron XPS studies have shown that edge carboxyls are much more easily removed than carbonyls, and phenolic C–OH, where the hydroxyl is attached to an sp^2 carbon, is the most stable [208]. Furthermore, the step at 600°C is accompanied by a large increase in the density of electrons near the Fermi level, which indicates the restoration of large sp2 regions and an increase in the rGO's conductivity.

Thermal reduction also results in exfoliation [209, 210] and a large increase in the pore sizes of rGO at 200–300°C, due to removal of gaseous species (H_2O, CO, CO_2, etc.) and oxygenated groups [211]. This is also seen in photothermal reduction, where exfoliation of graphene occurs at low laser fluences.

At 500–700°C the structure densifies slightly due to removal of hydroxyl or carbonyls, then becomes more open again at 900°C. Under the focus of a continuous wave or nanosecond laser, temperatures can reach in excess of 10^3–10^5K at the centre of a tightly focused beam [212]. In addition to exfoliation, defect healing is also observed at temperatures of 2000–2800°C via an annealing process. Both computational and experimental studies have pointed to vacancy elimination, increase of lateral domain size via cross-linking, and increase of hexagonal sp^2 regions, as the source of the defect elimination [213]. Full removal of defects has been observed for annealing at 2073K, if the starting GO material is already pre-reduced with a low concentration of oxygen functionalities that would otherwise desorb CO/CO_2 and leave behind vacancies [214]. Hence, photothermal reduction can increase the size of graphene domains and decrease the density of defects in rGO, relative to the starting GO.

Generally, laser reduction of GO in inert gas or vacuum conditions results in a higher quality rGO, with a greater electrical conductivity [133]. However, in thermal reduction of GO, reduction in hydrogen atmospheres has yielded more reduced rGO (higher C:O ratio) than reduction in inert argon atmospheres. This effect is possibly due to

the reduction by hydrogen of carbonyls and epoxides by to hydroxyl groups, which are then easily eliminated as water. For laser reduction of GO, the role of hydrogen gas can be replaced by strongly bound water molecules [215], that are retained in the initial desorption process of weakly intercalated water. Theoretical studies [216, 217] have indicated the plausibility of this mechanism, and further lends support to the importance of bound water in the reduction of GO. Molecular dynamics simulations are the primary source of insight into the atomistic mechanism, and advances in the computational efficiency of codes like LAMPSS and ReaxFF have enabled the simulation of larger flakes of GO.

Other than in aiding the exfoliation process, water intercalated within layers of GO can also play a role in the photoreduction process by changing the resulting optical properties of the rGO. The linear refractive index and absorption coefficient have both been found to increase upon thermal reduction of GO, due to the removal of water between GO layers. This can aid the further absorption of energy from the irradiation source and increase the conversion of GO to rGO [218].

8.4.2 Light–Matter Interaction Timescale in GO and LrGO

8.4.2.1 Continuous Wave Lasers

Continuous wave (CW) laser reduction is dominated by the photothermal reduction process for CW lasers in the IR and long wavelength regime (800 nm to 10 μm). Lazauskas *et al.* have shown similarities in the exfoliated morphology of rGO between LrGO at 788 nm, and that for thermally reduced GO [219]. Photochemical mechanisms can come into play if the wavelength of light exceeds the bandgap of GO (typically in the visible to near-UV energy range), and so is effectively absorbed.

Sokolov *et al.* have performed a comprehensive study investigating the mechanism of 405nm laser reduction with a single flake of GO [199]. The first step of the CW reduction process identified was photochemical in nature (Stage I in Figure 8.7a), as the measured temperature of the flakes did not change by more than a few Kelvin [220], and the activation energy for this step of the reduction process corresponds well to the barrier needed for elimination of a hydroxyl group. The next step is the reduction and ablation of rGO into a highly photoluminescent species after 100 seconds of irradiation with a 405 nm CW laser (Stage II in Figure 8.7a). The final stage is the photobleaching of the fragments due to excited state reactions of emissive species with oxygen. Heterogeneity in the extent of reduction is observed in the single GO flake, resulting from several factors; (i) the inherent disorder in the starting GO material, (ii) the laser beam profile, and (iii) temperature gradients due to inhomogeneous thermal conductivity that feed back to changes in photoinitiated events [220]. This can be seen by the superimposed photoluminescence rate of change vectors in Figure 8.7b–e. The rate of change vectors indicate the spread of the reduction, by tracking the gradient of photoluminescence intensity changes. The inhomogeneous spread of the "reduction front" can be decreased by rastering the laser beam. Hence, an optimal exposure time to the CW laser exists, which balances reduction of GO with photobleaching, an observation also made by Struchkov *et al.* [133].

The effect of fluence on the laser reduction process was studied by Deng *et al.* [119] with a 650 nm laser. The fluence dependence displays similar behavior to the effect of time on

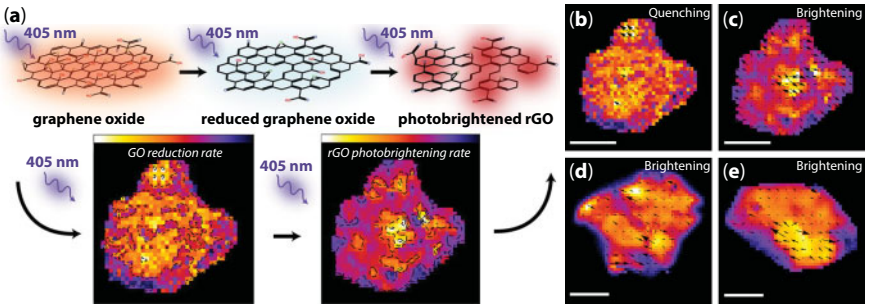

Figure 8.7 (a) Schematic showing continuous wave laser (405 nm) reduction of a single GO sheet, with color images below indicating the kinetics of reduction (Stage I) or photobrightening (Stage II) (measured by photoluminescence mapping). (b) Reduction vector field superimposed on top of a color map of the rate of photochemical reduction (c–e) Photoluminescence enhancement vector field superimposed on top of a color map of the rate of photoluminescence enhancement. All scale bars are 2.5 μm. Copyright 2013 American Chemical Society. Reproduced from [220] with permissions.

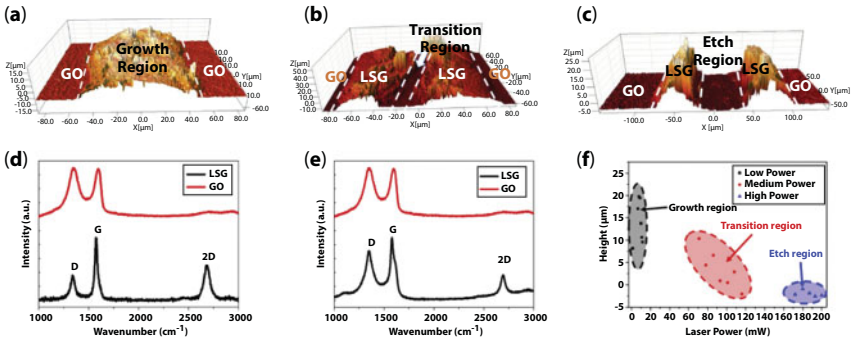

Figure 8.8 Topography map (from white light interferometry) of rGO in the (a) growth region, (b) transition region, and the (c) etch region. Corresponding Raman spectra are displayed below (d) growth region rGO (black) with GO (red) above, and (e) transition region rGO (black) and GO (red). (f) Height vs. laser power used, with the three regions classified. Copyright 2016 Elsevier. Reproduced from [119] with permissions.

reduction, suggesting a dependence of CW laser reduction on energy dosage rather than on fluence or time separately. They observe a clear growth region, where exfoliation and reduction to high quality rGO occurs (Figure 8.8a). The next stage is the transition region (Figure 8.8b), where the rGO layers are ablated in a layer-by-layer fashion with a concurrent decrease in the film thickness and increase in the size of the heat affected zone. The final region is the etch region, which is characterized by pure laser ablation of GO (Figure 8.8c). These three distinct regimes can be seen by correlating the height of the film relative to the laser power used (Figure 8.8f).

8.4.2.2 Nanosecond Pulsed Lasers

Nanosecond laser interaction in GO is also dominated by linear absorption, because of their high photon energy and long pulse duration, thus allowing the various photochemical processes detailed in Section 8.4.1.1 to occur. Nonlinear absorption can also

occur, mostly due to the absorption of the excited sp^3 and sp^2 states [27, 221], but with less efficiency than in femtosecond laser interaction. Depending on the wavelength of the laser, resonant excitation will result in excited state absorption, while non-resonant excitation will give multi-photon absorption. The absorption of photons by the GO sheets will allow the myriad photochemical processes related in Section 8.3.1.1 to occur.

With nanosecond laser treatment, there are further physical effects, due to the transient nature of the laser pulse. Once a photon is absorbed, the electron excitation will then thermalize to the lattice, and Sokolov *et al.* predict that hole–hole localization, exciton self-trapping, and material removal as a plasma may also occur [143]. The observation of ablation being concomitant with laser reduction is also observed by our group previously [122], especially during treatment in ambient atmosphere.

A pre-incubation effect is observed, where a minimum energy deposition is needed to initiate the removal of oxygen and create a certain density of vacancy defects, prior to material removal [122, 143]. Nanosecond laser pulse reduction of GO also produces a defined ablation plume. Sokolov *et al.* suggest that this ablation plume could contain carbon fragments that are re-oxidized in the presence of air and subsequently re-deposited on top of the material [143]. This could account for the lower quality of rGO produced by nanosecond laser treatment in air vs. in nitrogen [118]. However, later studies have shown that lasers can also photo-oxidize GO in addition to reducing it [193]. Hence, a balance may be struck between reduction and oxidation, especially in heterogeneous regions of the GO film that possess different degrees of oxygen functionalization.

8.4.2.3 Femtosecond Pulsed Lasers

The effect of femtosecond laser irradiation on GO is dominated by nonlinear effects, due to the high peak intensity of a pulse. The optical gap of GO lies between 2.6 to 3 eV [186]. As most femtosecond lasers operate in the Ti:sapphire wavelength of 800 nm (1.55 eV), the absorption of photons by GO is primarily nonlinear.

Numerous studies based on pump-probe spectroscopy with femtosecond laser pulses have been used to illustrate the ultrafast pre-reduction behavior of GO [186, 222, 223]. Murphy and Huang have studied the ultrafast behavior of GO films, and found a remarkable insensitivity of the excited state dynamics to the number of GO layers, substrate, and excitation intensity. This indicates the dominance of intra-layer electron dynamics and weak inter-layer interactions. They observe an initial 1–2 ps decay assigned to shallow defect trapping of electrons, and a longer decay lasting ~10–100 ps associated with non-radiative decay (e.g. thermalization with phonons, etc.).

High quality rGO has been made using high repetition rate femtosecond lasers, where incubation and heating effects can dominate [176]. Reduction with single pulses and low repetition rates (~1kHz) however, have not yielded high quality rGO, with a distinct Raman 2D band and small D band [184]. We interpret this as the effect of a decoupling between the photochemical removal of oxygen, and the subsequent relaxation of a sheet back into a planar form that is characteristic of graphene (and not other disordered forms of carbon).

Zhang and Miyamoto showed the possibility of selective breaking of C–O bonds, while keeping C–C bonds intact, using time dependent density functional theory models [224].

They demonstrated their simulations on a small nine carbon ring fragment, irradiated by a 800 nm, 2 fs pulse. These simulations showed the desorption of epoxy and hydroxy groups. However, all experimental demonstrations to date have been performed with longer pulses, >10 fs, and pulses with 10–45 fs durations can break the adhesive forces between graphene layers [224]. This is more in line with experimental cases, where laser reduction of GO is often performed with >1 layer of GO.

Irradiation of pristine graphene with a femtosecond laser at fluences below the ablation threshold was shown to introduce oxygen functionalities on the surface [193], which would compete with the nonlinear reduction process triggered by heating. Theoretical and STM studies have also shown that femtosecond laser irradiation of graphite can transform the sp^2 carbon on the surface into an sp^3 coordination, due to coherent excitation of interlayer compression and shear displacement [225]. This phenomenon is not observed with nanosecond pulsed laser irradiation of graphite, up to the ablation threshold [225].

On balance, these varied pieces of evidence point to the easy photochemical removal of oxygen, but the resulting rGO has a more disordered and non-planar structure. The non-planar structure can be relaxed by thermal annealing [101], for example due to incubation effects in high repetition rate, large pulse number irradiation treatments with femtosecond lasers [14, 180]. In contrast, the low quality rGO produced with single pulses, while "reduced" in the sense of having a lower oxygen content, lacks the structural features that distinguishes it as pristine graphene or rGO.

An exception to this hypothesis is the femtosecond laser reduction of GO while in aqueous solutions. In the case of UV photoreduction, contributions to the reduction process via thermal or photoionization of oxygen functionalities was ruled out [226]. The source of the electrons used for the reduction process instead was from the solvent (water) used. Over 1–250 ps, solvated electrons interacted with GO reducing it to rGO with several pulses being necessary for extensive reduction.

8.5 GO Synthesis and Characterization of Graphene Materials

8.5.1 Graphene Oxide Production

GO production is a field on its own, with many innovations in the production and surface deposition of GO over the past decade. Here, we will focus on the main methods of synthesis of GO, and review the various casting methodologies used to deposit graphene on surfaces. We also make some connections between the measured physical and chemical properties of GO to its subsequent behavior in laser reduction. This section is written as a "tutorial review" for readers unfamiliar with characterization and GO synthetic techniques. More advanced readers may skip this section.

8.5.1.1 Synthetic Routes to GO

The synthesis of GO and graphite oxide was launched by the publication of Brodie in 1885 [227], where concentrated H_2SO_4 and $KClO_3$ was used to oxidize graphite. However, the reagents used are extremely dangerous, and $KClO_3$ and H_2SO_4 can react to make ClO_2

which decomposes explosively at 45°C [228]. Many subsequent efforts to improve the process ensued [228], which culminated in three main methods to synthesize graphite oxide: the Staudenmaier, Hofmann, and Hummers–Offeman methods. Staudenmaier and Hoffmann's methods used HNO_3, H_2SO_4, and $KClO_3$ as the oxidizing agents, but at lower temperatures and different reagent ratios than the original synthesis proposed by Brodie. The low temperatures (managed by equipment like ice baths) are necessary to minimize the risk of explosions. The Hummers–Offeman method avoids the use of nitric acid and $KClO_3$ entirely, and uses concentrated H_2SO_4, $NaNO_3$, and $KMnO_4$. The resulting mixtures are often sedimented, centrifuged (to isolate uniform sheet sizes), and ultrasonicated in aqueous solvents to create a stable suspension of mono-disperse GO sheets. Care should be taken in the ultrasonication process to not over-sonicate and break up the lateral dimensions of the sheets [229]. For detailed descriptions of the synthesis of GO, we refer the readers to Refs. [103], [142], [230]. There are numerous modifications to the traditional synthetic procedures, such as the exfoliation of graphite sheets with intercalated ions [231], and an improved Hummers' method [232] to create a more oxidized product using H_2SO_4 and H_3PO_4 (without any $NaNO_3$).

The synthesis of GO is not a precise, atom-economic synthesis like in traditional organic synthesis. The combination of harsh oxidizing reagents used and poor control of the structure of the graphitic starting material often results in heterogeneous GOs being produced. This heterogeneity manifests in the sample morphology, ratio and location of functional groups (epoxides, carbonyls, carboxyls, etc.), and the density of defects. Further sources of sample heterogeneity originate from the workup process where the GO is isolated from the strong acid mixture, where the sample can be exposed to light or water. There is measurable difference in the heterogeneous electron transfer rates between thermally rGO made from GO synthesized by each of the three main techniques [228]. For electrochemical applications, the rGO originating from the Hummers' method shows faster electron transfer kinetics and lower overpotentials than the Staudenmaier or Hoffmann methods [230]. The oxidation mechanism of GO has been extensively studied both computationally and experimentally [100, 142, 233].

8.5.1.2 Surface Deposition of GO

GO holds primacy among graphene-based technologies due to its unique capability to be solution processed and hence coated onto a variety of substrates (e.g. SiO_2, Si, PET, ITO, metals, glassy carbon, polyimide, PTFE, etc.). GO is hydrophilic and hence dissolves easily in aqueous solvents. Upon ultrasonication, deposition, and drying, the resulting films can have controlled thicknesses and morphologies. There is an abundance of literature on the solution processing of GO, and this has been extensively reviewed [100, 234].

The important physical characteristic that makes GO so easily dispersible in aqueous solvents is its formally amphiphilic nature [235]. The basal plane of the sheet is composed of islands of hydrophobic unsaturated carbons, while the edges have a high concentration of hydrophilic oxygen functionalities. These oxygen groups serve to stabilize these sheets and solvation sites for water molecules.

Drop casting is the simplest method for the coating of GO onto various surfaces. It involves dropping a known volume of GO onto a surface and allowing it to dry in ambient conditions or under inert gas heating [236]. The thickness of films can be controlled by

changing the surface area/volume of GO deposited, or the concentration of the resulting solution. This method is versatile and allows coating on various substrate geometries and anisotropic structures. While the speed and ease of coating is advantageous, there is inhomogeneity in the thickness of the deposited film, due to surface tension effects. Furthermore, the quick drying of the surface layers of GO prevent water from escaping the layers below, thus increasing the amount of trapped water species [235]. The uniformity and hydrophobicity of drop-casted GO films can be tuned by modification of the underlying support substrate, for example by attaching oxygen functionalities to PET films [237].

Spin coating is a commonly used technique to create films of uniform thickness, where the thickness can be controlled by the viscosity of the solvent, the concentration of the solution, and the rotational speed of the spin coater. Spin coating can achieve very uniform and even monolayer thicknesses of GO and graphene on surfaces. Often, multiple stages of spin coating are required, to uniformly wet the surface and subsequently to thin the solvent layer. Nitrogen gas can also be simultaneously blown over the substrate while spinning, to increase the speed of solvent evaporation [238]. The downside to this quick sample preparation method is the time needed to optimize different spin coating parameters, and the substrate preparation. Spin coating substrates can vary depending on the application, but are often glass, silicon, or quartz. These substrates are often thoroughly cleaned in solvents like propanol or even piranha (mixture of H_2SO_4 and H_2O_2) solution before being coated. Furthermore, in order to create a more uniform coating of GO, functionalization of the surface with (aminopropyl)triethoxysilane [239] or oxygen plasma [240] can be performed. The oxo or silane groups increase the hydrophilicity of the surface, thus enabling GO to more efficiently wet the substrate. Subsequent drying of the GO solution can be done in a vacuum oven or in ambient conditions.

Vacuum filtration of a GO solution onto filter paper made of cellulose ester or polyamide is also common [74]. This procedure, which is commonly used to separate products in wet chemical synthesis, allows the deposition of thin films of GO from low concentration solutions. There is excellent control of the thickness (by varying concentration or filtration volume), as the deposition is self-limiting due to the lodging of GO sheets on the membrane's pores. However, as the pores are not uniform across the surface of the membrane, there is some inhomogeneity for the thin GO films deposited, because sheets that block nearby pores can overlap or cause wrinkles [74]. The resulting film can be kept on top of the membrane substrate, or can be delaminated for further use. The delamination can be performed by dissolving away the underlying membrane, and if pressed against another substrate, the GO film can be transferred over. The free-standing membrane can also be lifted off by water from the underlying substrate.

Other deposition methods include the Langmuir–Blodgett method, dip coating and spray coating [241] of a GO solution onto an inert substrate [100]. The Langmuir–Blodgett method involves spreading a solution of aqueous GO and methanol over water, thus suspending GO sheets at the air–water interface [235]. The layer is stable due to the reduction of surface tension of the surface by the GO monolayer, and the prevention of layer collapse by the electrostatic repulsion between the edge oxo-functionalities of the GO sheets. This film is then deposited onto a substrate and transferred over. There is potential for damage to the film during the transfer process, and careful solvent optimization, and speed of spreading is required.

8.5.2 Characterization and Quality Control Metrics for GO and Graphene Materials

Rational materials design is centered on the paradigm of understanding the relationship between structure, processing, properties, and performance. In order to understand this complicated relationship for LrGO materials, various characterization techniques are required. This is written in the style of a "tutorial review", to demonstrate the main advantages, limitations, and the important information that can be extracted using each technique.

The development of robust devices based on LrGO requires reliable and standardized metrics for quality. These metrics vary according to the application, and can be classified into microscopic parameters (Table 8.1) like defect density and crystallite size and macroscopic quantities (Table 8.2) like electrochemical reaction activity or electrical conductivity.

8.5.2.1 Morphology

Scanning electron microscopy (SEM) is used universally in materials science, and utilizes a raster scanned electron beam, and the electron–sample interactions, to generate an image.

Table 8.1 Microscopic parameters.

Microscopic parameter	Characterization techniques
Lateral sheet size	AFM, Raman, HRTEM
Defect concentration	Raman
Chemical composition (e.g. dopant, C:O ratio)	XPS, FTIR
Phase/impurities	TGA, UV-Vis
Layer structure	XRD, AFM, Raman
Surface morphology (wrinkles, etc.)	SEM, TEM, optical microscopy
Electronic structure (sp^2 conjugation)	UV-Vis

Table 8.2 Macroscopic quantities.

Macroscopic quantities	Characterization techniques
Surface area	BET, dye adsorption
Electrical conductivity	Four-point probe
Capacitance, electrode reaction kinetics	Cyclic voltammetry
Complex dielectric function	Electro-impedance spectroscopy
Optical absorbance, transmission, reflection	Spectroscopic ellipsometry

Although graphene layer thickness is smaller than the resolution of an SEM (typically nanometer), it can still reveal important information on the morphology of a graphene-based material.

The layered structure of graphene materials is a common observation in SEM characterization, and can be seen in seen in graphene, GO, and rGO in Figure 8.9. SEM can also be used to measure the lateral dimensions of graphene flakes, an important quality metric. Although it does not have the resolution required to measure graphene layer thickness, the appearance of "transparent" graphene flakes in SEM indicates the presence of few-layer graphene, with less than 10 graphene layers [242].

Transmission electron microscopy (TEM), high resolution electron microscopy (HR-TEM), and scanning transmission electron microscopy (STEM) are some of the most important characterization techniques for graphene-based materials. In conventional TEM, electron diffraction can be used to characterize the crystallinity of the underlying graphene lattice, which is maintained even when graphene is in an oxidized state [244]. The morphology of graphene flakes or platelets is also often observed, as well as wrinkles or folds in the film.

HR-TEM allows more detailed analysis of GO, due to its ability to image lattice atoms and defect sites. Domains of graphitic sp^2 carbons are typically seen, interspersed with regions where the pristine graphene structure is disrupted by oxygen moieties, as shown in Figure 8.10. The presence of these oxygen groups, and the structural disorder they introduce, are clearly seen by HR-TEM [245, 246]. In cross-sectional imaging, individual layers can be resolved, and layer spacing measured [247].

GO has also found application as a support film for TEM analysis of nanoparticles and macromolecules, due to its high electron transparency [244]. Practical concerns include the stability of GO under the high voltage beam, where oxidized groups are seen to move to where the electron beam is focused, leading to a upper limit for stable imaging of 60–80 kV [245].

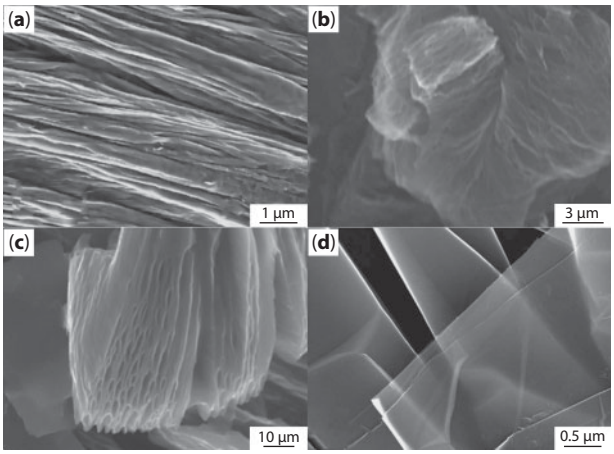

Figure 8.9 SEM images of graphene-based materials, including (a) GO, (b) LrGO, showing the layered structure created during laser-induced thermal exfoliation, (c) electrochemically exfoliated graphene, (d) "transparent" few-layer flakes of rGO. (a) and (d) reproduced with permission from [242]. Copyright 2012 Springer Nature. (c) reproduced from [243] under Creative Commons Attribution License (CC BY).

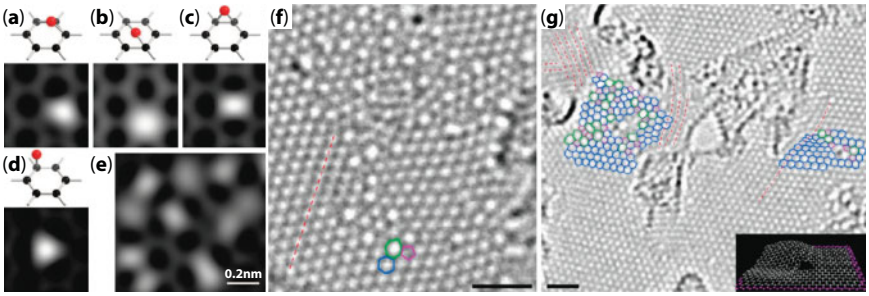

Figure 8.10 Left: Simulated STEM-ADF images of graphene with oxygen attached, (a–d) represent possible configurations of oxygen bonded to the graphene lattice, while (e) represents oxygen randomly connected to the graphene lattice in a 1:5 O:C ratio. Reproduced with permission from [15]. Copyright 2009 American Chemical Society. Middle and right: HR-TEM images of rGO showing graphene lattice and defects, with carbon hexagons (blue), pentagons (magenta), and heptagons (green) assigned. Reproduced with permission from [248]. Copyright 2010 American Chemical Society.

Contamination of GO with Si has also been observed in TEM images, a result of trace amounts of Si from deionized water filters being carried through the production process [245].

Brunauer–Emmett–Teller analysis (BET) determines the specific surface area of a sample (m^2/g) by measuring the amount of gas adsorbed on the sample surface. For graphene-based materials this metric has particular importance in the areas of sensors, supercapacitors, and hydrogen storage. Isolated graphene sheets have an extremely high surface area of 2630 m^2/g, however in practice surface areas greater than 700 m^2/g are rarely achieved due to agglomeration and presence of multilayer graphene. Modifications such as nanomesh graphene reduce this tendency, and have allowed specific surface areas of up to 1650 m^2/g to be achieved [249].

When analyzing graphene-based materials for capacitor applications, a number of practical limitations of the technique must be considered. Very narrow pores/cavities, such as those created by exfoliation of graphene layers, can be difficult to access by certain physisorbing gases, leading to discrepancies in specific surface area measured by N_2 and CO_2. This can lead to inconsistent or unreliable calculation of key performance metrics such as the interfacial capacitance (F/m^2) [250].

Optical microscopy is a widely used and relatively simple method for visually examining graphene-based materials. When placed on top of a certain thickness of SiO_2 on Si (dependent on illumination wavelength, 300 nm SiO_2 is used for white light), the path length difference means that even single layer graphene can be detected with a standard optical microscope, and contrast changes can be used to determine the number of layers present [251]. Recent advances have allowed optical microscopy to examine more than just the number of layers, and flake shape/size (Figure 8.11). Using selective oxidation of the underlying copper foil, grain boundaries in graphene sheets can be revealed under optical microscopy [252]. Interference reflectance microscopy (Figure 8.11), a label-free technique, can use the difference in refractive index between graphene and GO to watch the oxidation reaction progress [253].

Optical profilometry, or interferometry, is another optical technique that can provide information on the morphology of graphene-based materials, and has the added capability to give accurate information about changes in surface height by using an interference objective lens. Phase shifting interferometry uses a single wavelength source, and has

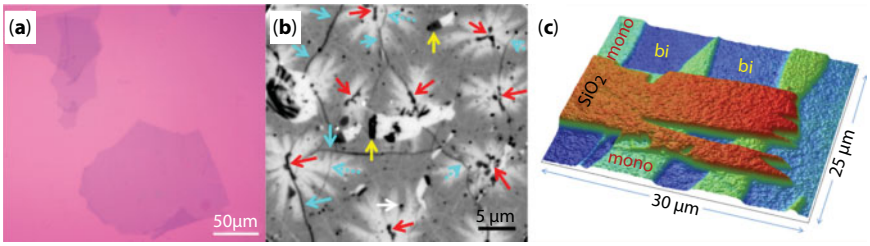

Figure 8.11 (a) Graphene on 300 nm SiO_2 illuminated at with white light, showing visibility of single and multilayer graphene. Reproduced with permission from [255]. Copyright 2010 American Chemical Society. (b) Interference reflectance microscopy image, showing graphene after 1h oxidation in Clorox, where lighter areas are oxidized graphene, initiated at nanoscale bilayers (red arrows). Reproduced with permission from [253]. Copyright 2017 American Chemical Society. (c) 3D phase shift interferometry image of graphene on SiO_2, showing how the phase shift through graphene appears as "recesses" in height data. Reproduced with permission from [254]. Copyright 2007 AIP Publishing.

extremely high vertical resolution (<0.1 nm) over a smoothly varying surface. Contrary to typical applications of this technique however, it is the phase shift of the light as it passes through the graphene layer, rather than the path length difference from reflection off the surface variations (graphene on silica has a very low reflectivity), that supplies the measured height differences. This means that height data appears inverted, with the phase shift from a graphene layer appearing to come from a recess relative to the surface (see Figure 8.11). To properly measure surface height, this must be calibrated using the known thickness of single layer graphene [254].

White light interferometry is another type of optical profilometry, where white light is used instead of a single wavelength, leading to lower vertical resolution (several nanometers) and increased range. White light interferometry relies on reflected light from the sample surface, so difficulties can arise when measuring graphene-based materials with low reflectivity. It is unable to resolve single graphene layers, but is useful for larger scale measurements, such as the thickness of films of graphene or GO cast from a solution.

Atomic force microscopy (AFM) uses a sharp, scanning tip to characterize the topography of insulating or conductive surfaces, making it ideal for imaging graphene, GO, and rGO. Key parameters measured with this technique include the lateral dimensions of graphene flakes, and layer thickness and number of layers, which are useful to assess the degree of exfoliation and agglomeration. The oxygenated groups on either side of the GO sheet typically give a single layer a thickness of around 1.2 nm, while the thickness of pristine graphene is 0.34 nm [245].

Shearer *et al.* discussed a number of factors that must be considered for accurate measurement of graphene, particularly relating to single layer graphene thickness. Firstly, an adsorbate layer is often present on top of the graphene layer which can affect tip–sample interactions—these are typically removed by laser irradiation. There is also evidence of a buffer layer between graphene and the substrate surface, the result of which is that the measured layer height is dependent on the pressure applied to the graphene. To obtain accurate layer thickness, the graphene must be pushed through the buffer layer to contact the surface, which can be done using high tip force, or modifications to the tip (such as attaching a carbon nanotube) to concentrate the force [256].

Scanning tunneling microscopy (STM) is a related technique that also makes use of a sharp scanning tip, but instead employs changes in the tunneling current between the tip and a conducting sample to build an image. It allows topography to be imaged with sub-atomic resolution, allowing graphene structure to be examined in detail [257]. Due to the insulating nature of GO, there are fewer studies using STM to characterize it, however Gómez-Navarro *et al.* report that oxidized regions appear as bright spots/regions, without ordered lattice features [258].

8.5.2.2 Chemical Structure

Raman spectroscopy is the pre-eminent technique for the analysis of carbon-based materials in general, and graphene in particular [259, 260]. Raman spectroscopy probes the quantized extended state vibrations (phonons) in graphene, and theoretical analysis allows classification of these vibrations by their symmetry. Shifts in the position of the peaks can be associated with strain in the lattice, and the full-width at half-maximum of the peaks is an indication of the disorder in the material [261, 262]. There are several bands visible in graphene-like materials, but we focus on three main ones [263], which can be seen in Figure 8.12 below. The G band (~1580 cm^{-1}) originates from an in-plane phonon with E_{2g} symmetry, and the 2D band (~2700 cm^{-1}) is linked to the planarity and electronic structure of graphene. In defective graphene-based materials, including GO and rGO, an additional peak called the D band (~1350 cm^{-1}) becomes prominent. The D band is a sp^2 ring-breathing

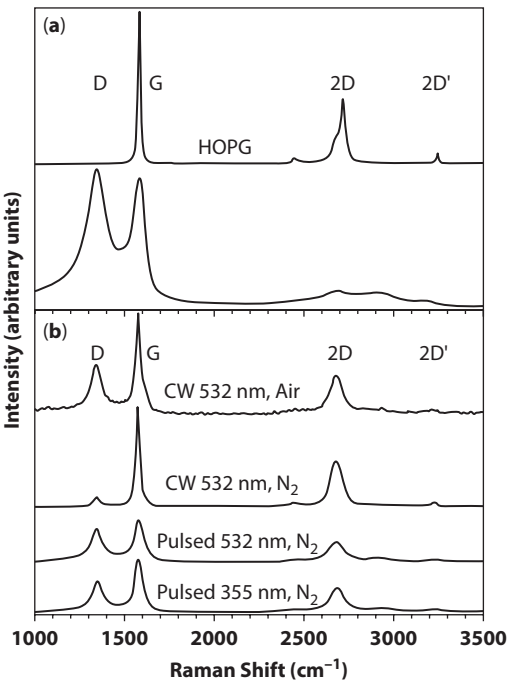

Figure 8.12 (a) Top: Raman spectrum of highly oriented pyrolytic graphite (HOPG) Bottom: Raman spectrum of GO, (b) Raman spectra of LrGO, with labels: continuous wave (CW), Pulsed nanosecond, and treated in air or N_2. Reproduced with permission from [118]. Copyright 2010 American Chemical Society.

mode with A_{1g} symmetry. The D-band is usually Raman inactive, except in the presence of disorder that changes it to a symmetry-allowed transition (atomic vacancies, grain boundaries, oxygen atoms, etc.).

Typically, Raman spectra of carbon materials are normalized to the G band, which is shared with other carbon based materials like carbon nanotubes and graphite [102]. Comparison between the Raman spectra of different photoreduction methods can be facilitated by this normalization. Subsequently, ratios of the intensity of the bands can be taken and correlated to different microscopic parameters. The I_{2D}/I_G ratio is related to the extent of graphenization [264], the I_D/I_G ratio is related to the defect density of the material, and the I_{2D}/I_D ratio indicates the number of layers (up to 5 layers, past which identification is difficult) [265].

Furthermore, the average crystallite size can be calculated from the I_D/I_G ratio, using the formula determined by Cançado *et al.* [266, 267]. While for monolayer graphene, a lower I_D/I_G ratio results in higher electronic conductivity, in multilayer or rGO materials, the reverse is often seen [134]. This is attributed to the increase in number of small graphene-like domains, thus increasing the conductivity relative to GO even though the domain sizes are smaller.

Charge inhomogeneity and impurities can also be detected for few-layer graphene in Raman spectra from peak shifts and widths [268].

Advances in instrumentation of micro-Raman and Raman mapping has allowed for spatially resolved maps of the degree of reduction of GO and insights into the mechanism of the reduction [136]. Upon laser irradiation of GO, successful establishment of graphene-like networks in rGO can be seen by the increase of the I_{2D}/I_G ratio, and if defect healing occurs, a decrease in the I_D/I_G ratio. However, in some applications, a high density of defects may still be useful, e.g. in electrochemical sensing. Care should be taken in the acquisition of the Raman spectrum of GO, as the laser power may inadvertently photoreduce it above a certain laser fluence threshold [269].

Fourier-transform infrared spectroscopy (FTIR) is an important tool for identifying different functional groups present in carbon based materials. Although pristine graphene itself does not have any functional groups with significant IR peaks, FTIR can give valuable information about the functional groups present in GO, rGO, and other types of functionalized graphene. For GO, the characteristic C–O peaks appear at 1050 cm^{-1} (epoxy C–O–C), 1680 cm^{-1} (–C=O vibration), 1350 cm^{-1} (C–O vibration), and 3470 cm^{-1} (C–OH stretch) [270]. For graphene-based materials, peaks lower than 900 cm^{-1} are not usually interpreted due to the complex structure they represent. C–C bonds can also be detected for graphene-based materials by FTIR, appearing at around 1500–1600 cm^{-1} [271].

The carbon:oxygen (C/O) ratio is a crucial metric when characterizing GO and rGO prepared by various methods, and **X-ray photoelectron spectroscopy** (XPS) is often used to measure this. GO typically has a C/O ratio in the range of 4:1–2:1, and after reduction this can be reduced to around 12:1 [104]. This type of elemental analysis is given in a low-resolution survey scan from the C1s/O1s peak area ratio; higher-resolution core level scans can give more detailed information on the different carbon functional groups present. Examples of survey and C1s core level spectra are shown in Figure 8.13 for GO, rGO, and graphite.

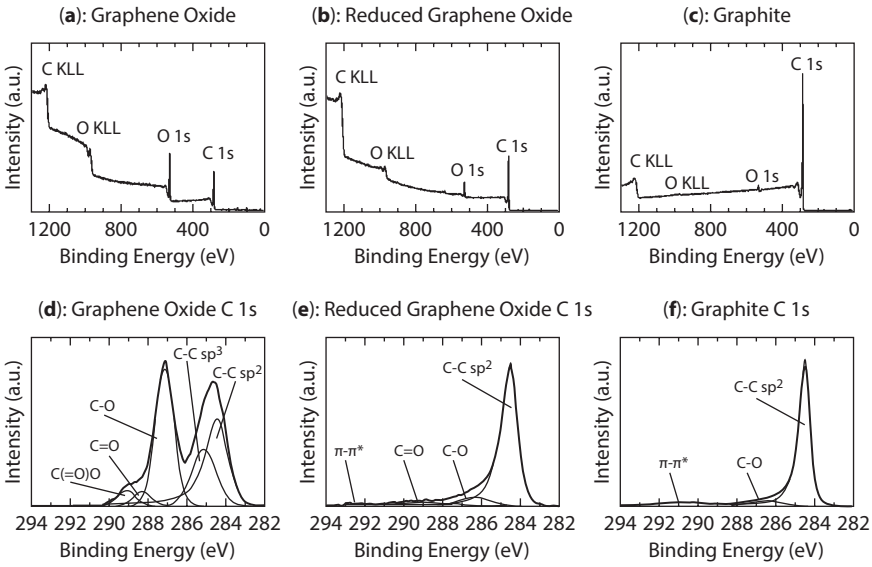

Figure 8.13 XPS spectra of GO (a, d), rGO (b, e), and graphite (c, f) showing survey scans (a–c) for elemental composition and C 1s core level scans (d–f) for carbon binding states.

In pure graphene, the C1s spectrum is dominated by the sp^2 bonding at ~284.6 eV, with additional π–π* transition peaks at >290 eV when there are large areas of pristine graphene lattice. When peak fitting graphene-based materials with high sp^2 content (*i.e.*, pristine graphene or highly reduced GO), the asymmetry of the sp^2 peak must also be considered, using a Doniach–Sunjic component [272]. If present, sp^3 carbon is found at ~285.4 eV, however these two C–C peaks can be difficult to deconvolute and are sometimes fit as one peak.

Measuring C–O components is crucial to analysis of GO, and the major components are C–O bonds at ~286.5 eV, encompassing epoxide (–O–) and hydroxyl (–OH) bonds, carbonyl bonds (C=O) at ~288 eV, and carboxyl bonds (C(=O)O) at ~289 eV. These groups appear prominently in GO and are present but much weaker in rGO. Doping graphene with nitrogen introduces additional peaks to the C1s spectra, most commonly found at ~258.8 eV and ~287.1 eV for sp^2 C=N and sp^3 C–N bonds respectively [273].

X-ray diffraction (XRD) analysis of graphene-based materials (usually in powder form) can reveal information about the interlayer spacing between graphitic layers. Pure graphite has its main peak at 26–27° (for Cu Kα radiation), corresponding to an interlayer spacing of about 3.35 Å. For GO, this peak is shifted to around 11°, but is influenced by the degree of oxidation and hydration, and interlayer spacing can vary between 6.0–9.5 Å (9–15°) [232, 270, 274]. Upon reduction of GO, this peak moves back to higher angle as the oxygen functional groups are removed, and graphene layers can pack more closely [275].

The Scherrer equation is often used with XRD data to calculate the crystallite size from peak width, and in most applications where the size of a crystallite is similar in all three dimensions, the Scherrer factor K is around 0.9. For graphene-based materials, the two-dimensional nature of graphene crystals must be taken into account, and the appropriate shape factor is 1.84, about twice as large [276].

8.5.2.3 *Electrical Properties*

The electrical conductivity of rGO is a measure of its quality [277, 278] as it is sensitive to the degree of oxygen reduction and defects in the graphene sheets. Mattevi [279] found comparable conductivities between films and individual flakes confirming that it is the quality of the rGO sheets themselves that mainly limit conductivity [234]. Indeed, multilayer stacks of rGO can have higher conductivities [280], since current can move between sheets to avoid defects on a single sheet.

rGO sheets are a disordered array of conducting sp^2 bonded carbons and insulating regions of sp^3 bonded oxidized carbon, or lattice defects. This was recently imaged directly using conductive atomic force microscopy [281, 282]. For typical residual oxygen fractions in rGO of <70% sp^2 bonded carbon, electronic conduction occurs due to tunneling of electrons between the conducting regions through the insulating regions [282, 283]. At higher oxygen reduction, percolation of the conducting sp^2 regions means that the conductivity approaches that of pure polycrystalline graphite, about 1e5 $S.m^{-1}$ [279].

Owing to its dependence on the degree of oxygen reduction, the resistivity of rGO can thus can be controlled by the reduction process. For example, for laser-rGO, the exposure time and intensity were used to vary the conductivity from the insulating GO (with its conductivity dominated by ionic conductivity [14]) up to 3e4 S/m [176].

8.5.2.4 *Optical Properties*

The optical response of rGO, described by the related quantities of the absorbance, transmittance, refractive index, complex conductivity, is an informative characteristic of rGO. It can be measured by techniques such as FTIR reflection or transmission spectroscopy, or more precisely by spectroscopic ellipsometry – a technique that also independently measures both the real and imaginary parts of the complex conductivity.

The reduction of GO can be characterized in a variety of ways in the optical response (Figure 8.14). Firstly, in the infra-red (IR) response, the transition from insulating GO to conducting rGO is marked by an increase in its optical absorption [284]. Additional information on the rGO quality, such as the carrier concentration and mobility, and Fermi-level, can be obtained from the complex conductivity, measured by spectroscopic ellipsometry [285].

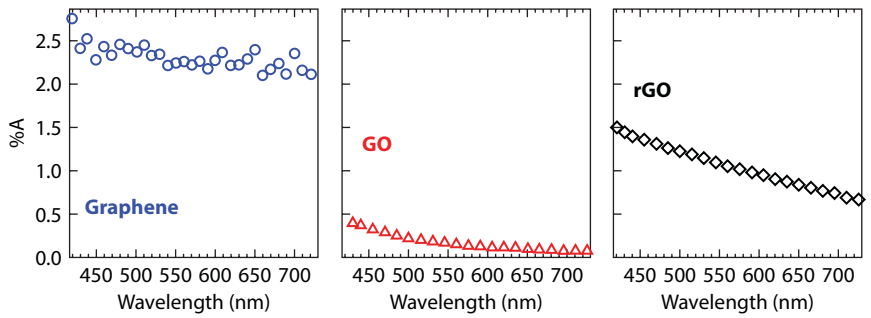

Figure 8.14 Absorbance spectra for graphene, GO, and rGO in the visible to near-IR region. Copyright 2015 Springer Nature. Reproduced from [284] with permissions.

The IR conductivity is also of interest as it reveals phonon excitations relating to the graphene, and impurities, such as hydroxyl and epoxy groups—which can be tracked before and after reduction of GO [284, 286].

At shorter wavelengths, in the visible and UV, pi–pi* interband transitions around 250 nm, are sensitive to the degree of rGO oxidation. Intercalated and adsorbed water is another impurity which can be measured, particularly well by ellipsometry, via both thickness of GO, and also its refractive index [287].

8.5.2.5 Electrochemical Properties

Graphene and graphene-based materials have shown huge promise in electrical power storage [66] and sensing [288]. Cyclic voltammetry is the leading technique used to characterize a candidate material for electrochemical applications. Cyclic voltammetry (CV) interrogates fundamental electron transfer (oxidation–reduction) processes between electrodes in contact with an electrolyte (liquid, gel, etc.). In essence, the technique involves applying a voltage sweep and monitoring the current response of the material to that voltage sweep. This sweep is performed at a certain voltage sweep rate, and the response of a material can vary as the sweep rate is changed (as in Figure 8.15a), depending on the kinetics of the electrochemical process. Peaks of the current vs. voltage response then give an indication as to the number and identity of chemical reactions occurring, either at the electrodes themselves or the solution surrounding the electrode. This principle can be used in sensing, as the voltage (relative to a standard like the standard calomel electrode, etc.) of a particular reaction can be characterized well. If a particular analyte undergoes a redox reaction at a certain voltage, the magnitude of the current of the oxidation or reduction peak can act as an indication of the concentration of the analyte in solution. The response of the analyte is then "piggybacked" or transduced through the graphene-based electrode and recorded on the CV trace [289], as in Figure 8.15b. We direct the reader to Refs [290] and [291] for a more comprehensive tutorial of the principles behind cyclic voltammetry.

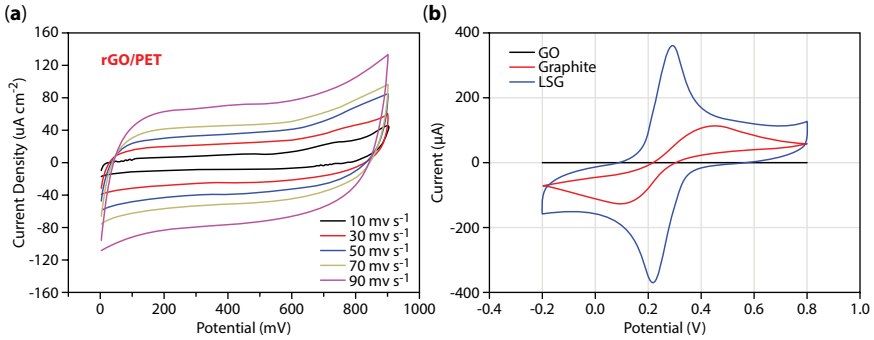

Figure 8.15 (a) Cyclic voltammogram of rGO supercapacitor on a PET substrate, at different voltage scan rates. Reproduced with permission from [124]. Copyright 2018 Elsevier. (b) Cyclic voltammogram of graphite oxide (G), graphite, and laser scribed graphene in a solution of $K_3[Fe(CN)_6]/K_4[Fe(CN)_6]$ dissolved in 1.0 M KCl at a 50 mV/s scan rate. Reproduced with permission from [120]. Copyright 2012 American Chemical Society.

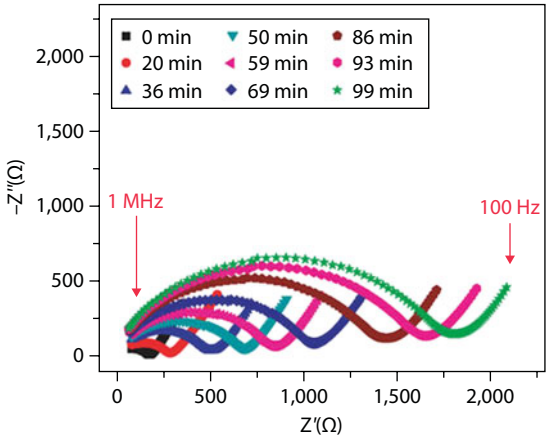

Figure 8.16 Electro-impedance spectrum of a pristine GO film at different exposure times to a vacuum at 25°C. Reproduced with permission from [14]. Copyright 2011 Springer Nature.

Differences in GO synthesis methods [292] and chemical reduction methods [41] give rise to different CV responses, and certain shapes may be more useful for certain applications. For example, a more box-like CV trace indicates a more capacitive response, and this helps characterize the capacitance value of the material [293].

Electro-impedance spectroscopy is a complementary technique to CV, and involves the application of a sinusoidal perturbation (or voltage or current) to a system, and monitoring the response at each frequency [294, 295]. From the frequency dependent potential and current, the complex impedance can be calculated. This data can be presented as a Bode plot (amplitude vs. frequency and phase vs. frequency) or as a Nyquist plot (complex impedance vs. real impedance). The response of the system can be modeled by circuit elements (like capacitors, resistances, etc.) and phenomenological models for chemical processes (e.g. Warburg diffusion elements [296], etc.). The complex impedance response can then be fitted to the model to extract useful parameters like double-layer capacitance and equivalent series resistance. The equivalent series resistance can indicate the speed of a capacitor's charge–discharge cycle. The impedance spectra can also be used to calculate the ionic conductivity of electrodes made of LrGO [14], and reveal the influence of water hydration and diffusion into the graphene sheets. Figure 8.16 shows the change in the shape of the electro-impedance spectrum of GO in the high frequency region, which corresponds to a decreased ionic conductivity as water is evaporated out over longer exposure to a vacuum environment [14].

8.6 Commercialization of Laser Reduced Graphene Oxide

The commercialization of graphene related materials (GRMs) is the goal of several concerted, and well-funded efforts around the world, from the USA to Europe to Korea [56]. Since the publication of its discovery in 2006, many companies (https://www.graphene-info.com/companies keeps an updated list of companies and news relating to graphene) entered into this space—some supplying research laboratories, but increasingly companies

using GRMs for in industrial and commercial applications [297]. The first major application of GRMs are thought to be from graphene–composite materials [298].

In terms of laser rGO, research interest has kept pace with GRMs (consistently accounting for about ~0.6% of papers) and about 60–70 related patents relating to laser rGO have been filed. However, unlike general GRMs, there are yet to be any clearly market ready products based on laser rGO. Since the processes are often proprietary, it can be difficult to know if a company incorporates laser rGO specifically in the production of their product! This is despite reports in academic literature of promising results [299].

The commercialization of laser rGO based products may be slowed because no one entity owns a significant number of those patents. There are also many challenges going from discovery to a market-ready product and is a process that generally takes several decades [298]. In this respect laser rGO technology is in fact still in its infancy since the first reports of laser rGO-based applications came out less than a decade ago in 2010–2011 ([300] and [301]).

Although there are currently no market-ready laser rGO products, (Figure 8.17) printed electronic circuits and on-chip supercapacitors are likely to be developed soon. rGO in general is an attractive material for use in supercapacitors (see Section 8.2.2.3) – and has been identified by many as key product to develop [299, 302]. Graphene-based supercapacitors are being marketed by called Skeleton Technologies and there are reports that CRRC, the Chinese state owned rolling stock manufacturer, is trailing graphene-based supercapacitors in public buses. The exact processes used by these manufacturers are not known, but it is likely a solution-processed rGO rather than laser rGO being used [68].

Prof. Kaner's group at Berkeley, who published early work on laser rGO-based supercapacitors, have since spun-out a company called NanoTech. This company makes and

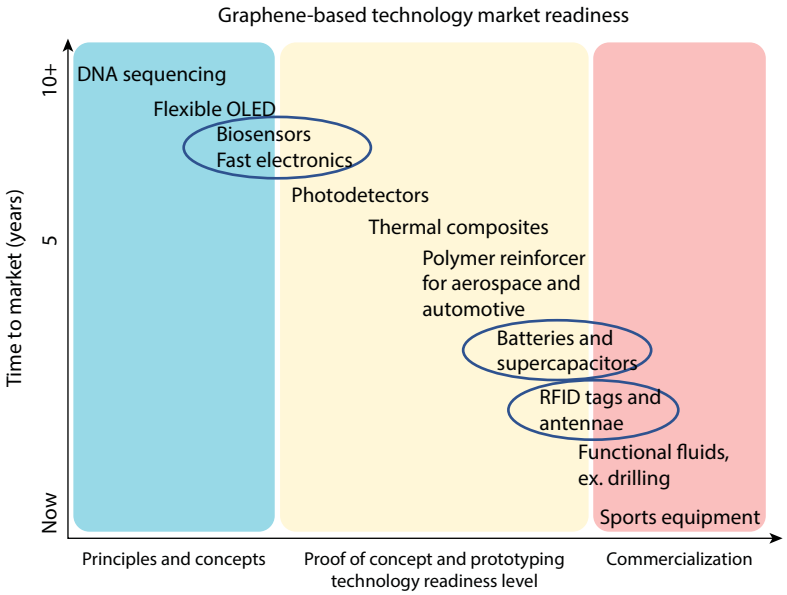

Figure 8.17 Estimates of readiness for various graphene-based technologies, with those where LrGO may play an important role circled. Copyright 2016 John Wiley and Sons. Reproduced from [56] with permissions.

sells rGO, using chemical, hydro- and photothermal methods to reduce GO. NanoTech is actively working to produce batteries, printed circuits and supercapacitors, but these applications are not yet market ready. The R&D at NanoTech is however indicative of a wider interest to develop laser rGO supercapacitors. For example Graphene Solutions is a recently formed company based on research from Swinburne University and which aims to make a prototype laser rGO supercapacitor by 2019.

The relatively young technology of laser rGO is likely to find commercial application given more development time. In the meantime, it can also play an important role in rapid prototyping and in R&D phase of some rGO products.

8.7 Conclusion

Graphene-based technologies have the potential to be widely integrated into the devices and infrastructure of the future. The fantastic electrical conductivity, electrochemical activity, surface area, and optoelectronic properties of graphene make it truly deserve its status as a "wonder material". Laser reduction of graphene oxide is one of the easiest and quickest methods to fabricate prototypes of graphene-based devices. It is a scalable technology, and research groups worldwide have raced to demonstrate its capabilities. However, this technology has yet to fully escape the confines of a research laboratory and enter industrial production. In order to push this technology into industry, applied research in the engineering of better laser reduced graphene oxide devices and basic research into the mechanism of the laser reduction process is required. In this chapter, we attempted to piece together spectroscopic and computational studies to create a model of the laser reduction process for a range of different pulsed and continuous wave lasers. There remain many unanswered questions and further experimental work probing the *in situ* chemical processes that occur during a femtosecond and nanosecond laser treatment is required. With a better understanding of these processes we anticipate the growing use of laser reduced graphene oxide as a common element within a materials scientist's and engineer's toolbox.

Acknowledgments

The authors would like to acknowledge support from the New Zealand Ministry of Business, Innovation and Employment (UOAX1202 and UOAX1416). RNO acknowledges funding and support from the Woolf Fisher Trust. BPPM acknowledges funding and support from the Rutherford Foundation of New Zealand.

References

1. Novoselov, K.S. *et al.*, Electric field effect in atomically thin carbon films. *Science*, 306, 5696, 666–669, 2004.
2. Geim, A.K. and Novoselov, K.S., The rise of graphene. *Nat. Mater.*, 6, 3, 183–191, 2007.
3. Zhang, Y. *et al.*, Experimental observation of the quantum Hall effect and Berry's phase in graphene. *Nature*, 438, 7065, 201, 2005.

4. Orlita, M. *et al.*, Approaching the Dirac point in high-mobility multilayer epitaxial graphene. *Phys. Rev. Lett.*, 101, 26, 267601, 2008.
5. Bolotin, K.I. *et al.*, Ultrahigh electron mobility in suspended graphene. *Solid State Commun.*, 146, 9, 351–355, 2008.
6. Du, X. *et al.*, Approaching ballistic transport in suspended graphene. *Nat. Nanotechnol.*, 3, 8, 491–495, 2008.
7. Wallace, P.R., The band theory of graphite. *Phys. Rev.*, 71, 9, 622–634, 1947.
8. Rao, C.e.N.e.R. *et al.*, Graphene: The new two-dimensional nanomaterial. *Angew. Chem. Int. Ed.*, 48, 42, 7752–7777, 2009.
9. Neto, A.C. *et al.*, The electronic properties of graphene. *Rev. Mod. Phys.*, 81, 1, 109, 2009.
10. Yazyev, O.V. and Louie, S.G., Electronic transport in polycrystalline graphene. *Nat. Mater.*, 9, 10, 806–809, 2010.
11. Dean, C.R. *et al.*, Boron nitride substrates for high-quality graphene electronics. *Nat. Nanotechnol.*, 5, 10, 722–726, 2010.
12. Schedin, F. *et al.*, Detection of individual gas molecules adsorbed on graphene. *Nat. Mater.*, 6, 9, 652–655, 2007.
13. El-Kady, M.F. and Kaner, R.B., Scalable fabrication of high-power graphene micro-supercapacitors for flexible and on-chip energy storage. *Nat. Commun.*, 4, 1475, 2013.
14. Gao, W. *et al.*, Direct laser writing of micro-supercapacitors on hydrated graphite oxide films. *Nat. Nanotechnol.*, 6, 8, 496–500, 2011.
15. Mkhoyan, K.A. *et al.*, Atomic and electronic structure of graphene-oxide. *NanoLett.*, 9, 3, 1058–1063, 2009.
16. Bonaccorso, F. *et al.*, Graphene photonics and optoelectronics. *Nat. Photonics*, 4, 9, 611–622, 2010.
17. Bao, Q. *et al.*, Atomic-layer graphene as a saturable absorber for ultrafast pulsed lasers. *Adv. Funct. Mater.*, 19, 19, 3077–3083, 2009.
18. Sun, Z. *et al.*, Graphene mode-locked ultrafast laser. *ACS Nano*, 4, 2, 803–810, 2010.
19. Husaini, S. and Bedford, R., Graphene saturable absorber for high power semiconductor disk laser mode-locking. *Appl. Phys. Lett.*, 104, 16, 161107, 2014.
20. Haus, H., Theory of mode locking with a slow saturable absorber. *IEEE J. Quantum Electron.*, 11, 9, 736–746, 1975.
21. Haus, H.A., Theory of mode locking with a fast saturable absorber. *J. Appl. Phys.*, 46, 7, 3049–3058, 1975.
22. Dean, J.J. and van Driel, H.M., Second harmonic generation from graphene and graphitic films. *Appl. Phys. Lett.*, 95, 26, 261910, 2009.
23. Mikhailov, S., Theory of the giant plasmon-enhanced second-harmonic generation in graphene and semiconductor two-dimensional electron systems. *Phys. Rev. B*, 84, 4, 045432, 2011.
24. Zhu, S. *et al.*, Surface chemistry routes to modulate the photoluminescence of graphene quantum dots: From fluorescence mechanism to up-conversion bioimaging applications. *Adv. Funct. Mater.*, 22, 22, 4732–4740, 2012.
25. Zhang, H. *et al.*, Z-scan measurement of the nonlinear refractive index of graphene. *Opt. Lett.*, 37, 11, 1856–1858, 2012.
26. Hendry, E. *et al.*, Coherent nonlinear optical response of graphene. *Phys. Rev. Lett.*, 105, 9, 097401, 2010.
27. Zheng, X. *et al.*, *In situ* third-order non-linear responses during laser reduction of graphene oxide thin films towards on-chip non-linear photonic devices. *Adv. Mater.*, 26, 17, 2699–2703, 2014.
28. Li, X., Zhang, Q., Chen, X., and Gu, M. (2013). Giant refractive-index modulation by two-photon reduction of fluorescent graphene oxides for multimode optical recording. *Sci. Rep.*, 3, 2819.

29. Loh, K.P. *et al.*, Graphene oxide as a chemically tunable platform for optical applications. *Nat. Chem.*, 2, 12, 1015–1024, 2010.
30. Nourbakhsh, A. *et al.*, Bandgap opening in oxygen plasma-treated graphene. *Nanotechnology*, 21, 43, 435203, 2010.
31. Gokus, T. *et al.*, Making graphene luminescent by oxygen plasma treatment. *ACS Nano*, 3, 12, 3963–3968, 2009.
32. Feng, Y. *et al.*, Enhancement in the fluorescence of graphene quantum dots by hydrazine hydrate reduction. *Carbon*, 66, 334–339, 2014.
33. Ju, J. and Chen, W., Synthesis of highly fluorescent nitrogen-doped graphene quantum dots for sensitive, label-free detection of Fe (III) in aqueous media. *Biosens. Bioelectron.*, 58, 219–225, 2014.
34. Shang, J. *et al.*, The origin of fluorescence from graphene oxide. *Sci. Rep.*, 2, 792, 2012.
35. Kim, J. *et al.*, Visualizing graphene based sheets by fluorescence quenching microscopy. *J. Am. Chem. Soc.*, 132, 1, 260–267, 2009.
36. Kagan, M.R. and McCreery, R.L., Reduction of fluorescence interference in Raman spectroscopy via analyte adsorption on graphitic carbon. *Anal. Chem.*, 66, 23, 4159–4165, 1994.
37. Xie, L. *et al.*, Graphene as a substrate to suppress fluorescence in resonance Raman spectroscopy. *J. Am. Chem. Soc.*, 131, 29, 9890–9891, 2009.
38. Brownson, D.A., and Banks, C.E., The handbook of graphene electrochemistry, pp. 127–174. London, Springer, 2014.
39. Chen, L. *et al.*, Direct electrodeposition of reduced graphene oxide on glassy carbon electrode and its electrochemical application. *Electrochem. Commun.*, 13, 2, 133–137, 2011.
40. Brownson, D.A. *et al.*, Electrochemistry of graphene: Not such a beneficial electrode material? *RSC Adv.*, 1, 6, 978–988, 2011.
41. Ambrosi, A. *et al.*, Graphene and its electrochemistry—An update. *Chem. Soc. Rev.*, 45, 9, 2458–2493, 2016.
42. Xiong, W. *et al.*, Direct writing of graphene patterns on insulating substrates under ambient conditions. *Sci. Rep.*, 4, 4892, 2014.
43. Bitounis, D. *et al.*, Prospects and challenges of graphene in biomedical applications. *Adv. Mater.*, 25, 16, 2258–2268, 2013.
44. Lee, E.J. *et al.*, Active control of all-fibre graphene devices with electrical gating. *Nat. Commun.*, 6, 6851, 2015.
45. Nieto, A. *et al.*, Graphene reinforced metal and ceramic matrix composites: A review. *Int. Mater. Rev.*, 62, 5, 241–302, 2017.
46. Kuilla, T. *et al.*, Recent advances in graphene based polymer composites. *Prog. Polym. Sci.*, 35, 11, 1350–1375, 2010.
47. O'Neill, A. *et al.*, Polymer nanocomposites: *In situ* polymerization of polyamide 6 in the presence of graphene oxide. *Polym. Compos.*, 38, 3, 528–537, 2017.
48. Young, R.J. *et al.*, The mechanics of graphene nanocomposites: A review. *Compos. Sci. Technol.*, 72, 12, 1459–1476, 2012.
49. Li, X. *et al.*, Graphene in photocatalysis: A review. *Small*, 12, 48, 6640–6696, 2016.
50. Prasai, D. *et al.*, Graphene: Corrosion-inhibiting coating. *ACS Nano*, 6, 2, 1102–1108, 2012.
51. Cui, C., Lim, A.T.O., Huang, J., A cautionary note on graphene anti-corrosion coatings. *Nat. Nanotechnol.*, 12, 9, 834–835, 2017.
52. Ambrosi, A. *et al.*, Electrochemistry of graphene and related materials. *Chem. Rev.*, 114, 14, 7150–7188, 2014.
53. Yang, Y. *et al.*, Graphene based materials for biomedical applications. *Mater. Today*, 16, 10, 365–373, 2013.
54. Rangel, N.L. and Seminario, J.M., Vibronics and plasmonics based graphene sensors. *J. Chem. Phys.*, 132, 12, 03B611, 2010.

55. Feng, L. *et al.*, A graphene functionalized electrochemical aptasensor for selective label-free detection of cancer cells. *Biomaterials*, 32, 11, 2930–2937, 2011.
56. Nazarpour, S. and Waite, S.R., *Graphene Technology: From Laboratory to Fabrication*, John Wiley & Sons, Hoboken, New Jersey, 2016.
57. Shao, Y. *et al.*, Graphene based electrochemical sensors and biosensors: A review. *Electroanalysis*, 22, 10, 1027–1036, 2010.
58. Pumera, M., Graphene in biosensing. *Mater. Today*, 14, 7, 308–315, 2011.
59. Koppens, F. *et al.*, Photodetectors based on graphene, other two-dimensional materials and hybrid systems. *Nat. Nanotechnol.*, 9, 10, 780–793, 2014.
60. Brownson, D.A., Kampouris, D.K., Banks, C.E., An overview of graphene in energy production and storage applications. *J. Power Sources*, 196, 11, 4873–4885, 2011.
61. Wolf, E.L., *Graphene: A New Paradigm in Condensed Matter and Device Physics*, OUP, Oxford, 2013.
62. Paek, S.-M., Yoo, E., Honma, I., Enhanced cyclic performance and lithium storage capacity of SnO2/graphene nanoporous electrodes with three-dimensionally delaminated flexible structure. *NanoLett.*, 9, 1, 72–75, 2008.
63. Wang, H. *et al.*, Mn3O4– graphene hybrid as a high-capacity anode material for lithium ion batteries. *J. Am. Chem. Soc.*, 132, 40, 13978–13980, 2010.
64. Zhou, G. *et al.*, Graphene-wrapped Fe3O4 anode material with improved reversible capacity and cyclic stability for lithium ion batteries. *Chem. Mater.*, 22, 18, 5306–5313, 2010.
65. Stoller, M.D. *et al.*, Graphene-Based Ultracapacitors. *NanoLett.*, 8, 10, 3498–3502, 2008.
66. El-Kady, M.F., Shao, Y., Kaner, R.B., Graphene for batteries, supercapacitors and beyond. *Nat. Rev. Mater.*, 1, 16033, 2016.
67. Shao, Y. *et al.*, Graphene-based materials for flexible supercapacitors. *Chem. Soc. Rev.*, 44, 11, 3639–3665, 2015.
68. Ke, Q. and Wang, J., Graphene-based materials for supercapacitor electrodes—A review. *J. Materiomics*, 2, 1, 37–54, 2016.
69. Wu, Z.-S., Feng, X., Cheng, H.-M., Recent advances in graphene-based planar micro-supercapacitors for on-chip energy storage. *Natl. Sci. Rev.*, 1, 2, 277–292, 2014.
70. Fiori, G. *et al.*, Electronics based on two-dimensional materials. *Nat. Nanotechnol.*, 9, 768, 2014.
71. Geim, A.K., Graphene: Status and prospects. *Science*, 324, 5934, 1530–1534, 2009.
72. Avouris, P. and Dimitrakopoulos, C., Graphene: Synthesis and applications. *Mater. Today*, 15, 3, 86–97, 2012.
73. Wassei, J.K. and Kaner, R.B., Graphene, a promising transparent conductor. *Mater. Today*, 13, 3, 52–59, 2010.
74. Eda, G., Fanchini, G., Chhowalla, M., Large-area ultrathin films of reduced graphene oxide as a transparent and flexible electronic material. *Nat. Nanotechnol.*, 3, 5, 270–274, 2008.
75. Novoselov, K.S. *et al.*, A roadmap for graphene. *Nature*, 490, 7419, 192–200, 2012.
76. Kim, J. and Song, Y., Ultralow-noise mode-locked fiber lasers and frequency combs: Principles, status, and applications. *Adv. Opt. Photonics*, 8, 3, 465–540, 2016.
77. Sun, Z. *et al.*, A stable, wideband tunable, near transform-limited, graphene-mode-locked, ultrafast laser. *Nano Res.*, 3, 9, 653–660, 2010.
78. Zhang, H. *et al.*, Graphene mode locked, wavelength-tunable, dissipative soliton fiber laser. *Appl. Phys. Lett.*, 96, 11, 111112, 2010.
79. Ma, J. *et al.*, Graphene mode-locked femtosecond laser at 2 μm wavelength. *Opt. Lett.*, 37, 11, 2085–2087, 2012.
80. Zhu, G. *et al.*, Graphene mode-locked fiber laser at 2.8$\mu\text {m} $. *IEEE Photonics Technol. Lett.*, 28, 1, 7–10, 2016.

81. Cho, W.B. *et al.*, Graphene mode-locked femtosecond Cr 2+: ZnS laser with ~300 nm tuning range. *Opt. Express*, 24, 18, 20774–20780, 2016.
82. Wang, X., Tian, H., Mohammad, M. A., Li, C., Wu, C., Yang, Y., & Ren, T. L. (2015). A spectrally tunable all-graphene-based flexible field-effect light-emitting device. *Nature communications*, 6, 7767.
83. Shen, H. *et al.*, Biomedical applications of graphene. *Theranostics*, 2, 3, 283, 2012.
84. Yang, K. *et al.*, Nano-graphene in biomedicine: Theranostic applications. *Chem. Soc. Rev.*, 42, 2, 530–547, 2013.
85. Chang, H. *et al.*, Graphene fluorescence resonance energy transfer aptasensor for the thrombin detection. *Anal. Chem.*, 82, 6, 2341–2346, 2010.
86. Balapanuru, J. *et al.*, A graphene oxide–organic dye ionic complex with dna-sensing and optical-limiting properties. *Angew. Chem.*, 122, 37, 6699–6703, 2010.
87. Zhang, Y., Zhang, L., Zhou, C., Review of chemical vapor deposition of graphene and related applications. *Acc. Chem. Res.*, 46, 10, 2329–2339, 2013.
88. Zhang, H. and Feng, P.X., Fabrication and characterization of few-layer graphene. *Carbon*, 48, 2, 359–364, 2010.
89. Kumar, I. and Khare, A., Multi-and few-layer graphene on insulating substrate via pulsed laser deposition technique. *Appl. Surf. Sci.*, 317, 1004–1009, 2014.
90. Qian, M. *et al.*, Formation of graphene sheets through laser exfoliation of highly ordered pyrolytic graphite. *Appl. Phys. Lett.*, 98, 17, 173108, 2011.
91. Koh, A.T., Foong, Y.M., Chua, D.H., Comparison of the mechanism of low defect few-layer graphene fabricated on different metals by pulsed laser deposition. *Diamond Relat. Mater.*, 25, 98–102, 2012.
92. Damm, C., Nacken, T.J., Peukert, W., Quantitative evaluation of delamination of graphite by wet media milling. *Carbon*, 81, 284–294, 2015.
93. Ciesielski, A. and Samorì, P., Graphene via sonication assisted liquid-phase exfoliation. *Chem. Soc. Rev.*, 43, 1, 381–398, 2014.
94. Su, C.-Y. *et al.*, High-quality thin graphene films from fast electrochemical exfoliation. *ACS Nano*, 5, 3, 2332–2339, 2011.
95. Varrla, E. *et al.*, Turbulence-assisted shear exfoliation of graphene using household detergent and a kitchen blender. *Nanoscale*, 6, 20, 11810–11819, 2014.
96. Lotya, M. *et al.*, Liquid phase production of graphene by exfoliation of graphite in surfactant/water solutions. *J. Am. Chem. Soc.*, 131, 10, 3611–3620, 2009.
97. Ang, P.K. *et al.*, High-throughput synthesis of graphene by intercalation–exfoliation of graphite oxide and study of ionic screening in graphene transistor. *ACS Nano*, 3, 11, 3587–3594, 2009.
98. Coleman, J.N., Liquid exfoliation of defect-free graphene. *Acc. Chem. Res.*, 46, 1, 14–22, 2012.
99. Yi, M. and Shen, Z., A review on mechanical exfoliation for the scalable production of graphene. *J. Mater. Chem. A*, 3, 22, 11700–11715, 2015.
100. Eda, G. and Chhowalla, M., Chemically derived graphene oxide: Towards large-area thin-film electronics and optoelectronics. *Adv. Mater.*, 22, 22, 2392–2415, 2010.
101. Gao, W. *et al.*, New insights into the structure and reduction of graphite oxide. *Nat. Chem.*, 1, 5, 403–408, 2009.
102. Liu, W.-W. *et al.*, Synthesis and characterization of graphene and carbon nanotubes: A review on the past and recent developments. *J. Ind. Eng. Chem.*, 20, 4, 1171–1185, 2014.
103. Eigler, S. and Hirsch, A., Chemistry with graphene and graphene oxide—Challenges for synthetic chemists. *Angew. Chem. Int. Ed.*, 53, 30, 7720–7738, 2014.
104. Pei, S. and Cheng, H.-M., The reduction of graphene oxide. *Carbon*, 50, 9, 3210–3228, 2012.
105. Zhou, M. *et al.*, Controlled synthesis of large-area and patterned electrochemically reduced graphene oxide films. *Chem. Eur. J.*, 15, 25, 6116–6120, 2009.

106. Gao, X., Jang, J., Nagase, S., Hydrazine and thermal reduction of graphene oxide: Reaction mechanisms, product structures, and reaction design. *J. Phys. Chem. C*, 114, 2, 832–842, 2009.
107. Guo, H.-L. *et al.*, A green approach to the synthesis of graphene nanosheets. *ACS Nano*, 3, 9, 2653–2659, 2009.
108. Zhou, Y. *et al.*, Hydrothermal dehydration for the "green" reduction of exfoliated graphene oxide to graphene and demonstration of tunable optical limiting properties. *Chem. Mater.*, 21, 13, 2950–2956, 2009.
109. Zhu, Y. *et al.*, Microwave assisted exfoliation and reduction of graphite oxide for ultracapacitors. *Carbon*, 48, 7, 2118–2122, 2010.
110. Liu, R. *et al.*, A catalytic microwave process for superfast preparation of high-quality reduced graphene oxide. *Angew. Chem.*, 129, 49, 15883–15888, 2017.
111. Voiry, D. *et al.*, High-quality graphene via microwave reduction of solution-exfoliated graphene oxide. *Science*, 353, 6306, 1413–1416, 2016.
112. Chaban, V.V. and Prezhdo, O.V., Microwave reduction of graphene oxide rationalized by reactive molecular dynamics. *Nanoscale*, 9, 11, 4024–4033, 2017.
113. Guo, H. *et al.*, Preparation of reduced graphene oxide by infrared irradiation induced photothermal reduction. *Nanoscale*, 5, 19, 9040–9048, 2013.
114. Guardia, L. *et al.*, UV light exposure of aqueous graphene oxide suspensions to promote their direct reduction, formation of graphene–metal nanoparticle hybrids and dye degradation. *Carbon*, 50, 3, 1014–1024, 2012.
115. Orabona, E. *et al.*, Holographic patterning of graphene-oxide films by light-driven reduction. *Opt. Lett.*, 39, 14, 4263–4266, 2014.
116. Sadallaha, F. and Elsaida, E.A., Novel optical technique for 2D graphene reduction, in: *Proc. of SPIE Vol*, 2017.
117. Zhou, Y. *et al.*, Microstructuring of graphene oxide nanosheets using direct laser writing. *Adv. Mater.*, 22, 1, 67–71, 2010.
118. Sokolov, D.A., Shepperd, K.R., Orlando, T.M., Formation of graphene features from direct laser-induced reduction of graphite oxide. *J. Phys. Chem. Lett.*, 1, 18, 2633–2636, 2010.
119. Deng, N.-Q. *et al.*, Tunable graphene oxide reduction and graphene patterning at room temperature on arbitrary substrates. *Carbon*, 109, 173–181, 2016.
120. Strong, V. *et al.*, Patterning and electronic tuning of laser scribed graphene for flexible all-carbon devices. *ACS Nano*, 6, 2, 1395–1403, 2012.
121. El-Kady, M.F. *et al.*, Laser scribing of high-performance and flexible graphene-based electrochemical capacitors. *Science*, 335, 6074, 1326–1330, 2012.
122. Arul, R. *et al.*, The mechanism of direct laser writing of graphene features into graphene oxide films involves photoreduction and thermally assisted structural rearrangement. *Carbon*, 99, 423–431, 2016.
123. Wang, D. *et al.*, Laser induced self-propagating reduction and exfoliation of graphite oxide as an electrode material for supercapacitors. *Electrochim. Acta*, 141, 271–278, 2014.
124. Ghoniem, E., Mori, S., Abdel-Moniem, A., Low-cost flexible supercapacitors based on laser reduced graphene oxide supported on polyethylene terephthalate substrate. *J. Power Sources*, 324, 272–281, 2016.
125. Hu, Y. *et al.*, All-in-one graphene fiber supercapacitor. *Nanoscale*, 6, 12, 6448–6451, 2014.
126. Cheng, H. *et al.*, Graphene fibers with predetermined deformation as moisture-triggered actuators and robots. *Angew. Chem. Int. Ed.*, 52, 40, 10482–10486, 2013.
127. Xu, G. *et al.*, Direct laser scribed graphene/PVDF-HFP composite electrodes with improved mechanical water wear and their electrochemistry. *Appl. Mater. Today*, 8, 35–43, 2017.
128. Teoh, H.F. *et al.*, Microlandscaping on a graphene oxide film via localized decoration of Ag nanoparticles. *Nanoscale*, 6, 6, 3143–3149, 2014.

129. Wan, Y. *et al.*, Spontaneous decoration of Au nanoparticles on micro-patterned reduced graphene oxide shaped by focused laser beam. *J. Appl. Phys.*, 117, 5, 054304, 2015.
130. Lee, W.H. *et al.*, Selective-area fluorination of graphene with fluoropolymer and laser irradiation. *NanoLett.*, 12, 5, 2374–2378, 2012.
131. Liu, J. *et al.*, Modulated deformation of lipid membrane to vesicles and tubes due to reduction of graphene oxide substrate under laser irradiation. *Carbon*, 98, 300–306, 2016.
132. Zhang, T.-Y. *et al.*, A super flexible and custom-shaped graphene heater. *Nanoscale*, 9, 38, 14357–14363, 2017.
133. Struchkov, N. *et al.*, Research and development of the method of graphene oxide thin films local reduction by modulated laser irradiation, in: *Journal of Physics: Conference Series*, IOP Publishing, Bristol, 2017.
134. Furio, A. *et al.*, Light irradiation tuning of surface wettability, optical, and electric properties of graphene oxide thin films. *Nanotechnology*, 28, 5, 054003, 2016.
135. Longo, A. *et al.*, Graphene oxide prepared by graphene nanoplatelets and reduced by laser treatment. *Nanotechnology*, 28, 22, 224002, 2017.
136. Eigler, S., Dotzer, C., Hirsch, A., Visualization of defect densities in reduced graphene oxide. *Carbon*, 50, 10, 3666–3673, 2012.
137. Ye, R., Chyan, Y., Zhang, J., Li, Y., Han, X., Kittrell, C., and Tour, J. M., Laser-induced graphene formation on wood. *Adv. Mater.*, 29, 37, 1702211, 2017.
138. Chen, L. *et al.*, Fabrication of rGO-GO long period fiber grating using laser reduction method. *IEEE Photonics J.*, 9, 6, 1–9, 2017.
139. Kondrashov, V.A. *et al.*, Graphene oxide reduction by solid-state laser irradiation for bolometric applications. *Nanotechnology*, 29, 3, 035301, 2017.
140. Qiao, Z. *et al.*, Versatile and scalable micropatterns on graphene oxide films based on laser induced fluorescence quenching effect. *Opt. Express*, 25, 25, 31025–31035, 2017.
141. Gamil, M. *et al.*, Graphene-based strain gauge on a flexible substrate. *Sens. Mater.*, 26, 9, 699–709, 2014.
142. Dreyer, D.R. *et al.*, The chemistry of graphene oxide. *Chem. Soc. Rev.*, 39, 1, 228–240, 2010.
143. Sokolov, D.A. *et al.*, Excimer laser reduction and patterning of graphite oxide. *Carbon*, 53, 81–89, 2013.
144. Le Borgne, V. *et al.*, Hydrogen-assisted pulsed KrF-laser irradiation for the *in situ* photoreduction of graphene oxide films. *Carbon*, 77, 857–867, 2014.
145. Yung, K. *et al.*, Laser direct patterning of a reduced-graphene oxide transparent circuit on a graphene oxide thin film. *J. Appl. Phys.*, 113, 24, 244903, 2013.
146. Yung, W.K. *et al.*, Eye-friendly reduced graphene oxide circuits with nonlinear optical transparency on flexible poly (ethylene terephthalate) substrates. *J. Mater. Chem. C*, 3, 43, 11294–11299, 2015.
147. Lin, T. *et al.*, Laser-ablation production of graphene oxide nanostructures: From ribbons to quantum dots. *Nanoscale*, 7, 6, 2708–2715, 2015.
148. Guan, Y. *et al.*, Fabrication of laser-reduced graphene oxide in liquid nitrogen environment. *Sci. Rep.*, 6, 28913, 2016.
149. Bhaumik, A. and Narayan, J., Wafer scale integration of reduced graphene oxide by novel laser processing at room temperature in air. *J. Appl. Phys.*, 120, 10, 105304, 2016.
150. Huang, L. *et al.*, Pulsed laser assisted reduction of graphene oxide. *Carbon*, 49, 7, 2431–2436, 2011.
151. Abdelsayed, V. *et al.*, Photothermal deoxygenation of graphite oxide with laser excitation in solution and graphene-aided increase in water temperature. *J. Phys. Chem. Lett.*, 1, 19, 2804–2809, 2010.

152. Liu, Y. *et al.*, Pulsed laser assisted reduction of graphene oxide as a flexible transparent conducting material. *J. Nanosci. Nanotechnol.*, 12, 8, 6480–6483, 2012.
153. Kumar, P., Subrahmanyam, K., Rao, C., Graphene produced by radiation-induced reduction of graphene oxide. *Int. J. Nanosci.*, 10, 04n05, 559–566, 2011.
154. Ghadim, E.E. *et al.*, Pulsed laser irradiation for environment friendly reduction of graphene oxide suspensions. *Appl. Surf. Sci.*, 301, 183–188, 2014.
155. Spanò, S.F. *et al.*, Tunable properties of graphene oxide reduced by laser irradiation. *Appl. Phys. A*, 117, 1, 19–23, 2014.
156. Wang, S. *et al.*, The role of sp 2/sp 3 hybrid carbon regulation in the nonlinear optical properties of graphene oxide materials. *RSC Adv.*, 7, 84, 53643–53652, 2017.
157. Li, H. *et al.*, Photoreduction of graphene oxide with polyoxometalate clusters and its enhanced saturable absorption. *J. Colloid Interface Sci.*, 427, 25–28, 2014.
158. Anwar, A. *et al.*, Simple and inexpensive synthesis of rGO-(Ag, Ni) nanocomposites via green methods. *Mater. Technol.*, 30, sup3, 155–160, 2015.
159. Russo, P. *et al.*, In liquid laser treated graphene oxide for dye removal. *Appl. Surf. Sci.*, 348, 85–91, 2015.
160. Filice, S. *et al.*, Modification of graphene oxide and graphene oxide–TiO 2 solutions by pulsed laser irradiation for dye removal from water. *Mater. Sci. Semicond. Process.*, 42, 50–53, 2016.
161. Li, L. *et al.*, Reduced TiO2-graphene oxide heterostructure as broad spectrum-driven efficient water-splitting photocatalysts. *ACS Appl. Mater. Interfaces*, 8, 13, 8536–8545, 2016.
162. Queraltó, A. *et al.*, MAPLE synthesis of reduced graphene oxide/silver nanocomposite electrodes: Influence of target composition and gas ambience. *J. Alloys Compd.*, 726, 1003–1013, 2017.
163. del Pino, A.P. *et al.*, Study of the deposition of graphene oxide by matrix-assisted pulsed laser evaporation. *J. Phys. D: Appl. Phys.*, 46, 50, 505309, 2013.
164. György, E. *et al.*, Titanium oxide–reduced graphene oxide–silver composite layers synthesized by laser technique: Wetting and electrical properties. *Ceram. Int.*, 42, 14, 16191–16197, 2016.
165. Jiang, H.B. *et al.*, Bioinspired fabrication of superhydrophobic graphene films by two-beam laser interference. *Adv. Funct. Mater.*, 24, 29, 4595–4602, 2014.
166. Wang, J.N. *et al.*, Biomimetic graphene surfaces with superhydrophobicity and iridescence. *Chem. Asian J.*, 7, 2, 301–304, 2012.
167. Savva, K. *et al.*, *In situ* photo-induced chemical doping of solution-processed graphene oxide for electronic applications. *J. Mater. Chem. C*, 2, 29, 5931–5937, 2014.
168. Ryu, B.D. *et al.*, Stimulated N-doping of reduced graphene oxide on GaN under excimer laser reduction process. *Mater. Lett.*, 116, 412–415, 2014.
169. Bhaumik, A. and Narayan, J., Conversion of p to n-type reduced graphene oxide by laser annealing at room temperature and pressure. *J. Appl. Phys.*, 121, 12, 125303, 2017.
170. Yun, X. *et al.*, Hierarchical porous graphene film: An ideal material for laser-carving fabrication of flexible micro-supercapacitors with high specific capacitance. *Carbon*, 125, 308–317, 2017.
171. Kumar, R. *et al.*, Direct laser writing of micro-supercapacitors on thick graphite oxide films and their electrochemical properties in different liquid inorganic electrolytes. *J. Colloid Interface Sci.*, 507, 271–278, 2017.
172. Das, S.R. *et al.*, 3D nanostructured inkjet printed graphene via UV-pulsed laser irradiation enables paper-based electronics and electrochemical devices. *Nanoscale*, 8, 35, 15870–15879, 2016.
173. Evlashin, S. *et al.*, Controllable laser reduction of graphene oxide films for photoelectronic applications. *ACS Appl. Mater. Interfaces*, 8, 42, 28880–28887, 2016.
174. Konios, D. *et al.*, Reduced graphene oxide micromesh electrodes for large area, flexible, organic photovoltaic devices. *Adv. Funct. Mater.*, 25, 15, 2213–2221, 2015.

175. Yan, R. *et al.*, An abnormal non-incubation effect in femtosecond laser processing of free-standing reduced graphene oxide paper. *J. Phys. D: Appl. Phys.*, 50, 18, 185302, 2017.
176. Zhang, Y. *et al.*, Direct imprinting of microcircuits on graphene oxides film by femtosecond laser reduction. *Nano Today*, 5, 1, 15–20, 2010.
177. Chang, H.-W. *et al.*, Reduction of graphene oxide in aqueous solution by femtosecond laser and its effect on electroanalysis. *Electrochem. Commun.*, 23, 37–40, 2012.
178. Trusovas, R. *et al.*, Reduction of graphite oxide to graphene with laser irradiation. *Carbon*, 52, 574–582, 2013.
179. Kymakis, E. *et al.*, Flexible organic photovoltaic cells with *in situ* nonthermal photoreduction of spin-coated graphene oxide electrodes. *Adv. Funct. Mater.*, 23, 21, 2742–2749, 2013.
180. Kasischke, M. *et al.*, Graphene oxide reduction induced by femtosecond laser irradiation, in: *Nanostructured Thin Films X, International Society for Optics and Photonics*, Washington, 2017.
181. Guo, L. *et al.*, Laser-mediated programmable n doping and simultaneous reduction of graphene oxides. *Adv. Opt. Mater.*, 2, 2, 120–125, 2014.
182. Bi, Y.-G. *et al.*, Arbitrary shape designable microscale organic light-emitting devices by using femtosecond laser reduced graphene oxide as a patterned electrode. *ACS Photonics*, 1, 8, 690–695, 2014.
183. Zheng, X., Jia, B., Lin, H., Qiu, L., Li, D., and Gu, M., Highly efficient and ultra-broadband graphene oxide ultrathin lenses with three-dimensional subwavelength focusing. *Nat. Commun.*, 6, 8433, 2015.
184. Li, X. *et al.*, Athermally photoreduced graphene oxides for three-dimensional holographic images. *Nat. Commun.*, 6, 6984, 2015.
185. Gattass, R.R. and Mazur, E., Femtosecond laser micromachining in transparent materials. *Nat. Photonics*, 2, 4, 219, 2008.
186. Liaros, N. *et al.*, Ultrafast processes in graphene oxide during femtosecond laser excitation. *J. Phys. Chem. C*, 120, 7, 4104–4111, 2016.
187. Mao, S., Pu, H., Chen, J., Graphene oxide and its reduction: Modeling and experimental progress. *RSC Adv.*, 2, 7, 2643–2662, 2012.
188. Lerf, A. *et al.*, Structure of graphite oxide revisited. *J. Phys. Chem. B*, 102, 23, 4477–4482, 1998.
189. De Jesus, L.R. *et al.*, Inside and outside: X-ray absorption spectroscopy mapping of chemical domains in graphene oxide. *J. Phys. Chem. Lett.*, 4, 18, 3144–3151, 2013.
190. Rodriguez-Pastor, I. *et al.*, Towards the understanding of the graphene oxide structure: How to control the formation of humic-and fulvic-like oxidized debris. *Carbon*, 84, 299–309, 2015.
191. Erickson, K. *et al.*, Determination of the local chemical structure of graphene oxide and reduced graphene oxide. *Adv. Mater.*, 22, 40, 4467–4472, 2010.
192. Hong, Y.-Z. *et al.*, Reduction-oxidation dynamics of oxidized graphene: Functional group composition dependent path to reduction. *Carbon*, 129, 396–402, 2018.
193. Koivistoinen, J. *et al.*, From seeds to islands: Growth of oxidized graphene by two-photon oxidation. *J. Phys. Chem. C*, 120, 39, 22330–22341, 2016.
194. Maiti, R. *et al.*, Tunable optical properties of graphene oxide by tailoring the oxygen functionalities using infrared irradiation. *Nanotechnology*, 25, 49, 495704, 2014.
195. Larciprete, R. *et al.*, Dual path mechanism in the thermal reduction of graphene oxide. *J. Am. Chem. Soc.*, 133, 43, 17315–17321, 2011.
196. Plotnikov, V. *et al.*, The graphite oxide photoreduction mechanism. *High Energy Chem.*, 45, 5, 411–415, 2011.
197. Matsumoto, Y. *et al.*, Simple photoreduction of graphene oxide nanosheet under mild conditions. *ACS Appl. Mater. Interfaces*, 2, 12, 3461–3466, 2010.
198. Minella, M. *et al.*, Photochemical stability and reactivity of graphene oxide. *J. Mater. Sci.*, 50, 6, 2399–2409, 2015.

199. Sokolov, D.A. *et al.*, Direct observation of single layer graphene oxide reduction through spatially resolved, single sheet absorption/emission microscopy. *NanoLett.*, 14, 6, 3172–3179, 2014.
200. Shulga, Y.M. *et al.*, Gaseous products of thermo-and photo-reduction of graphite oxide. *Chem. Phys. Lett.*, 498, 4, 287–291, 2010.
201. Gurvich, L. *et al.*, Energii razryva khimicheskikh svyazei. Potentsialy ionizatsii i srodstvo k elektronu, in: *Bond Dissociation Energies, Ionization Potentials, and Electron Affinity*, V.N. Kondrat'ev (Ed.), Nauka, Moscow, 1974.
202. Smirnov, V. *et al.*, Photochemical processes in graphene oxide films. *High Energy Chem.*, 50, 1, 51–59, 2016.
203. Coyle, J.D., *Introduction to Organic Photochemistry*, John Wiley & Sons, Hoboken, New Jersey, 1986.
204. Shi, H. *et al.*, Tuning the nonlinear optical absorption of reduced graphene oxide by chemical reduction. *Opt. Express*, 22, 16, 19375–19385, 2014.
205. Liaros, N. *et al.*, The effect of the degree of oxidation on broadband nonlinear absorption and ferromagnetic ordering in graphene oxide. *Nanoscale*, 8, 5, 2908–2917, 2016.
206. Perumbilavil, S. *et al.*, White light Z-scan measurements of ultrafast optical nonlinearity in reduced graphene oxide nanosheets in the 400–700 nm region. *Appl. Phys. Lett.*, 107, 5, 051104, 2015.
207. Karimzadeh, R. and Arandian, A., Unusual nonlinear absorption response of graphene oxide in the presence of a reduction process. *Laser Phys. Lett.*, 12, 2, 025401, 2014.
208. Ganguly, A. *et al.*, Probing the thermal deoxygenation of graphene oxide using high-resolution *in situ* X-ray-based spectroscopies. *J. Phys. Chem. C*, 115, 34, 17009–17019, 2011.
209. Barroso-Bujans, F., Alegría, A., Colmenero, J., Kinetic study of the graphite oxide reduction: Combined structural and gravimetric experiments under isothermal and nonisothermal conditions. *J. Phys. Chem. C*, 114, 49, 21645–21651, 2010.
210. McAllister, M.J. *et al.*, Single sheet functionalized graphene by oxidation and thermal expansion of graphite. *Chem. Mater.*, 19, 18, 4396–4404, 2007.
211. Dolbin, A.V. *et al.*, The effect of the thermal reduction temperature on the structure and sorption capacity of reduced graphene oxide materials. *Appl. Surf. Sci.*, 361, 213–220, 2016.
212. Bäuerle, D., *Laser Processing and Chemistry*, Springer Science & Business Media, Heidelberg, 2013.
213. Huang, Y. *et al.*, Fabrication and molecular dynamics analyses of highly thermal conductive reduced graphene oxide films at ultra-high temperatures. *Nanoscale*, 9, 6, 2340–2347, 2017.
214. Rozada, R. *et al.*, From graphene oxide to pristine graphene: Revealing the inner workings of the full structural restoration. *Nanoscale*, 7, 6, 2374–2390, 2015.
215. Buchsteiner, A., Lerf, A., Pieper, J., Water dynamics in graphite oxide investigated with neutron scattering. *J. Phys. Chem. B*, 110, 45, 22328–22338, 2006.
216. Acik, M. *et al.*, The role of intercalated water in multilayered graphene oxide. *ACS Nano*, 4, 10, 5861–5868, 2010.
217. Cabrera-Sanfelix, P. and Darling, G.R., Dissociative adsorption of water at vacancy defects in graphite. *J. Phys. Chem. C*, 111, 49, 18258–18263, 2007.
218. Jung, I. *et al.*, Characterization of thermally reduced graphene oxide by imaging ellipsometry. *J. Phys. Chem. C*, 112, 23, 8499–8506, 2008.
219. Lazauskas, A. *et al.*, Thermally-driven structural changes of graphene oxide multilayer films deposited on glass substrate. *Superlattices Microstruct.*, 75, 461–467, 2014.
220. McDonald, M.P. *et al.*, Direct observation of spatially heterogeneous single-layer graphene oxide reduction kinetics. *NanoLett.*, 13, 12, 5777–5784, 2013.

221. Liu, Z. *et al.*, Nonlinear optical properties of graphene oxide in nanosecond and picosecond regimes. *Appl. Phys. Lett.*, 94, 2, 021902, 2009.
222. Zhang, Q. *et al.*, The realistic domain structure of as-synthesized graphene oxide from ultrafast spectroscopy. *J. Am. Chem. Soc.*, 135, 33, 12468–12474, 2013.
223. Murphy, S. and Huang, L., Transient absorption microscopy studies of energy relaxation in graphene oxide thin film. *J. Phys.: Condens. Matter*, 25, 14, 144203, 2013.
224. Zhang, H. and Miyamoto, Y., Graphene production by laser shot on graphene oxide: An *ab initio* prediction. *Phys. Rev. B*, 85, 3, 033402, 2012.
225. Kanasaki, J. *et al.*, Formation of s p 3-bonded carbon nanostructures by femtosecond laser excitation of graphite. *Phys. Rev. Lett.*, 102, 8, 087402, 2009.
226. Gengler, R.Y. *et al.*, Revealing the ultrafast process behind the photoreduction of graphene oxide. *Nat. Commun.*, 4, 2560, 2013.
227. Brodie, B.C., On the atomic weight of graphite. *Philos. Trans. R. Soc. London*, 149, 249–259, 1859.
228. Dimiev, A.M., *Graphene Oxide: Fundamentals and Applications*, John Wiley & Sons, Hoboken, New Jersey, 2016.
229. Eda, G. and Chhowalla, M., Graphene-based composite thin films for electronics. *NanoLett.*, 9, 2, 814–818, 2009.
230. Poh, H.L. *et al.*, Graphenes prepared by Staudenmaier, Hofmann and Hummers methods with consequent thermal exfoliation exhibit very different electrochemical properties. *Nanoscale*, 4, 11, 3515–3522, 2012.
231. Zheng, Q. *et al.*, Graphene oxide-based transparent conductive films. *Prog. Mater. Sci.*, 64, 200–247, 2014.
232. Marcano, D.C. *et al.*, Improved synthesis of graphene oxide. *ACS Nano*, 4, 8, 4806–4814, 2010.
233. Gao, X. *et al.*, Theoretical insights into the structures of graphene oxide and its chemical conversions between graphene. *J. Comput. Theor. Nanosci.*, 8, 12, 2406–2422, 2011.
234. Parviz, D. *et al.*, Challenges in liquid-phase exfoliation, processing, and assembly of pristine graphene. *Adv. Mater.*, 28, 40, 8796–8818, 2016.
235. Kim, F., Cote, L.J., Huang, J., Graphene oxide: Surface activity and two-dimensional assembly. *Adv. Mater.*, 22, 17, 1954–1958, 2010.
236. Li, D. *et al.*, Processable aqueous dispersions of graphenenanosheets. *Nat. Nanotechnol.*, 3, 2, 101–105, 2008.
237. Zhao, C. *et al.*, Formation of uniform reduced graphene oxide films on modified PET substrates using drop-casting method. *Particuology*, 17, 66–73, 2014.
238. Robinson, J.T. *et al.*, Reduced graphene oxide molecular sensors. *NanoLett.*, 8, 10, 3137–3140, 2008.
239. Becerril, H.A. *et al.*, Evaluation of solution-processed reduced graphene oxide films as transparent conductors. *ACS Nano*, 2, 3, 463–470, 2008.
240. Yang, D. *et al.*, Chemical analysis of graphene oxide films after heat and chemical treatments by X-ray photoelectron and Micro-Raman spectroscopy. *Carbon*, 47, 1, 145–152, 2009.
241. Pham, V.H. *et al.*, Fast and simple fabrication of a large transparent chemically-converted graphene film by spray-coating. *Carbon*, 48, 7, 1945–1951, 2010.
242. Tkachev, S.V. *et al.*, Reduced graphene oxide. *Inorg. Mater.*, 48, 8, 796–802, 2012.
243. Cooper, A.J. *et al.*, Single stage electrochemical exfoliation method for the production of few-layer graphene via intercalation of tetraalkylammonium cations. *Carbon*, 66, 340–350, 2014.
244. Wilson, N.R. *et al.*, Graphene oxide: Structural analysis and application as a highly transparent support for electron microscopy. *ACS Nano*, 3, 9, 2547–2556, 2009.
245. Gao, W., *Graphene Oxide: Reduction Recipes, Spectroscopy, and Applications*, Springer, Cham, 2015.

246. Zhao, J., Liu, L., Li, F., *Graphene Oxide: Physics and Applications*, Springer, Amsterdam, 2015.
247. Moon, I.K. *et al.*, Reduced graphene oxide by chemical graphitization. *Nat. Commun.*, 1, 73, 2010.
248. Gómez-Navarro, C. *et al.*, Atomic structure of reduced graphene oxide. *NanoLett.*, 10, 4, 1144–1148, 2010.
249. Ning, G. *et al.*, Gram-scale synthesis of nanomesh graphene with high surface area and its application in supercapacitor electrodes. *Chem. Commun.*, 47, 21, 5976–5978, 2011.
250. Lobato, B. *et al.*, Capacitance and surface of carbons in supercapacitors. *Carbon*, 122, 434–445, 2017.
251. Blake, P. *et al.*, Making graphene visible. *Appl. Phys. Lett.*, 91, 6, 063124, 2007.
252. Duong, D.L. *et al.*, Probing graphene grain boundaries with optical microscopy. *Nature*, 490, 7419, 235–239, 2012.
253. Wojcik, M. *et al.*, Spatially resolved *in situ* reaction dynamics of graphene via optical microscopy. *J. Am. Chem. Soc.*, 139, 16, 5836–5841, 2017.
254. Venkatachalam, D.K. *et al.*, Rapid, substrate-independent thickness determination of large area graphene layers. *Appl. Phys. Lett.*, 99, 23, 234106, 2011.
255. Zhao, J. *et al.*, Efficient preparation of large-area graphene oxide sheets for transparent conductive films. *ACS Nano*, 4, 9, 5245–5252, 2010.
256. Shearer, C.J. *et al.*, Accurate thickness measurement of graphene. *Nanotechnology*, 27, 12, 125704, 2016.
257. Andrei, E.Y., Li, G., Du, X., Electronic properties of graphene: A perspective from scanning tunneling microscopy and magnetotransport. *Rep. Prog. Phys.*, 75, 5, 056501, 2012.
258. Gómez-Navarro, C. *et al.*, Electronic transport properties of individual chemically reduced graphene oxide sheets. *NanoLett.*, 7, 11, 3499–3503, 2007.
259. Ferrari, A.C. and Basko, D.M., Raman spectroscopy as a versatile tool for studying the properties of graphene. *Nat. Nanotechnol.*, 8, 4, 235–246, 2013.
260. Malard, L. *et al.*, Raman spectroscopy in graphene. *Phys. Rep.*, 473, 5, 51–87, 2009.
261. Pimenta, M. *et al.*, Studying disorder in graphite-based systems by Raman spectroscopy. *Phys. Chem. Chem. Phys.*, 9, 11, 1276–1290, 2007.
262. Ferrari, A.C., Raman spectroscopy of graphene and graphite: Disorder, electron–phonon coupling, doping and nonadiabatic effects. *Solid State Commun.*, 143, 1, 47–57, 2007.
263. Kudin, K.N. *et al.*, Raman spectra of graphite oxide and functionalized graphene sheets. *NanoLett.*, 8, 1, 36–41, 2008.
264. Ferrari, A.C. and Robertson, J., Interpretation of Raman spectra of disordered and amorphous carbon. *Phys. Rev. B*, 61, 20, 14095, 2000.
265. Faugeras, C. *et al.*, Few-layer graphene on SiC, pyrolitic graphite, and graphene: A Raman scattering study. *Appl. Phys. Lett.*, 92, 1, 011914, 2008.
266. Cançado, L. *et al.*, General equation for the determination of the crystallite size La of nanographite by Raman spectroscopy. *Appl. Phys. Lett.*, 88, 16, 163106, 2006.
267. Cançado, L.G. *et al.*, Quantifying defects in graphene via Raman spectroscopy at different excitation energies. *NanoLett.*, 11, 8, 3190–3196, 2011.
268. Casiraghi, C. *et al.*, Raman fingerprint of charged impurities in graphene. *Appl. Phys. Lett.*, 91, 23, 233108, 2007.
269. Mehta, J.S. *et al.*, How reliable are Raman spectroscopy measurements of graphene oxide? *J. Phys. Chem. C*, 121, 30, 16584–16591, 2017.
270. Lee, D. *et al.*, The structure of graphite oxide: Investigation of its surface chemical groups. *J. Phys. Chem. B*, 114, 17, 5723–5728, 2010.
271. Krishnamoorthy, K. *et al.*, The chemical and structural analysis of graphene oxide with different degrees of oxidation. *Carbon*, 53, 38–49, 2013.

272. Speranza, G. and Minati, L., The surface and bulk core lines in crystalline and disordered polycrystalline graphite. *Surf. Sci.*, 600, 19, 4438–4444, 2006.
273. Susi, T., Pichler, T., Ayala, P., X-ray photoelectron spectroscopy of graphitic carbon nanomaterials doped with heteroatoms. *Beilstein J. Nanotechnol.*, 6, 177, 2015.
274. Szabó, T., Berkesi, O., Dékány, I., DRIFT study of deuterium-exchanged graphite oxide. *Carbon*, 43, 15, 3186–3189, 2005.
275. Stobinski, L. *et al.*, Graphene oxide and reduced graphene oxide studied by the XRD, TEM and electron spectroscopy methods. *J. Electron Spectrosc. Relat. Phenom.*, 195, 145–154, 2014.
276. Warren, B., X-ray diffraction in random layer lattices. *Phys. Rev.*, 59, 9, 693, 1941.
277. Luo, D. *et al.*, Evaluation criteria for reduced graphene oxide. *J. Phys. Chem. C*, 115, 23, 11327–11335, 2011.
278. Zhu, Y. *et al.*, Graphene and graphene oxide: Synthesis, properties, and applications. *Adv. Mater.*, 22, 35, 3906–3924, 2010.
279. Mattevi, C. *et al.*, Evolution of electrical, chemical, and structural properties of transparent and conducting chemically derived graphene thin films. *Adv. Funct. Mater.*, 19, 16, 2577–2583, 2009.
280. Tu, Y. *et al.*, Enhancing the electrical conductivity of vacuum-ultraviolet-reduced graphene oxide by multilayered stacking. *J. Vac. Sci. Technol., B: Nanotechnol. Microelectron.*, 35, 3, 03D110, 2017.
281. Tu, Y. *et al.*, Vacuum-ultraviolet photoreduction of graphene oxide: Electrical conductivity of entirely reduced single sheets and reduced micro line patterns. *Appl. Phys. Lett.*, 106, 13, 133105, 2015.
282. Faucett, A.C. *et al.*, Evolution, structure, and electrical performance of voltage-reduced graphene oxide. *FlatChem*, 1, 42–51, 2017.
283. Joung, D., Zhai, L., Khondaker, S.I., Coulomb blockade and hopping conduction in graphene quantum dots array. *Phys. Rev. B*, 83, 11, 115323, 2011.
284. McDonald, M.P., Morozov, Y., Hodak, J.H., and Kuno, M., Spectroscopy and microscopy of graphene oxide and reduced graphene oxide, in: *Graphene Oxide: Reduction Recipes, Spectroscopy, and Applications*, Springer, Cham., pp. 29–60, 2015.
285. Chang, Y.C. *et al.*, Extracting the complex optical conductivity of mono- and bilayer graphene by ellipsometry. *Appl. Phys. Lett.*, 104, 26, 261909, 2014.
286. Malek Hosseini, S.M.B. *et al.*, Excimer laser assisted very fast exfoliation and reduction of graphite oxide at room temperature under air ambient for Supercapacitors electrode. *Appl. Surf. Sci.*, 427, 507–516, 2018.
287. Ghosh, M. *et al.*, Confined water layers in graphene oxide probed with spectroscopic ellipsometry. *Appl. Phys. Lett.*, 106, 24, 241902, 2015.
288. Hill, E.W., Vijayaragahvan, A., Novoselov, K., Graphene sensors. *IEEE Sens. J.*, 11, 12, 3161–3170, 2011.
289. Griffiths, K. *et al.*, Laser-scribed graphene presents an opportunity to print a new generation of disposable electrochemical sensors. *Nanoscale*, 6, 22, 13613–13622, 2014.
290. Elgrishi, N., Rountree, K.J., McCarthy, B.D., Rountree, E.S., Eisenhart, T.T., and Dempsey, J.L., A practical beginner's guide to cyclic voltammetry. *J. Chem. Educ.*, 95(2), 197–206, 2017.
291. Mabbott, G.A., An introduction to cyclic voltammetry. *J. Chem. Educ.*, 60, 9, 697, 1983.
292. Eng, A.Y.S. *et al.*, Unusual inherent electrochemistry of graphene oxides prepared using permanganate oxidants. *Chem. Eur. J.*, 19, 38, 12673–12683, 2013.
293. Li, R.-Z. *et al.*, High-rate in-plane micro-supercapacitors scribed onto photo paper using *in situ* femtolaser-reduced graphene oxide/Au nanoparticle microelectrodes. *Energy Environ. Sci.*, 9, 4, 1458–1467, 2016.

294. Orazem, M.E. and Tribollet, B., *Electrochemical Impedance Spectroscopy*, vol. 48, John Wiley & Sons, Hoboken, New Jersey, 2011.
295. Barsoukov, E. and Macdonald, J.R., *Impedance Spectroscopy: Theory, Experiment, and Applications*, John Wiley & Sons, Hoboken, New Jersey, 2005.
296. Li, F. *et al.*, All-solid-state potassium-selective electrode using graphene as the solid contact. *Analyst*, 137, 3, 618–623, 2012.
297. Ciriminna, R. *et al.*, Commercialization of graphene-based technologies: A critical insight. *Chem. Commun.*, 51, 33, 7090–7095, 2015.
298. Park, S., The puzzle of graphene commercialization. *Nat. Rev. Mater.*, 1, 16085, 2016.
299. Kumar, R., Singh, R.K., Singh, D.P., Joanni, E., Yadav, R.M., and Moshkalev, S.A., Laser-assisted synthesis, reduction and micro-patterning of graphene: Recent progress and applications. *Coord. Chem. Rev.*, 342, 34–79, 2017.
300. Duocastella, M. and Arnold, C.B., Bessel and annular beams for materials processing. *Laser Photonics Rev.*, 6, 5, 607–621, 2012.
301. El-Kady, M.F., Strong, V.A., and Kaner, R.B. U.S. Patent No. 9,779,884. Washington, DC: U.S. Patent and Trademark Office, 2017.
302. Ferrari, A.C. *et al.*, Science and technology roadmap for graphene, related two-dimensional crystals, and hybrid systems. *Nanoscale*, 7, 11, 4598–4810, 2015.